ANNUAL REVIEWS **Further**

Click here for quick links to Annual Reviews content online, including:

- Other articles in this volume
- Top cited articles
- Top downloaded articles
- Our comprehensive search

Chemical Expansion: Implications for Electrochemical Energy Storage and Conversion Devices

S.R. Bishop,[1,2,*,§] D. Marrocchelli,[3,4,*] C. Chatzichristodoulou,[5,*] N.H. Perry,[1,2] M.B. Mogensen,[5] H.L. Tuller,[1,2] and E.D. Wachsman[6]

[1]International Institute for Carbon Neutral Energy Research (WPI-I2CNER), Kyushu University, Fukuoka 819-0395, Japan; email: bishop@i2cner.kyushu-u.ac.jp, perry@i2cner.kyushu-u.ac.jp

[2]Department of Materials Science and Engineering, Massachusetts Institute of Technology, Cambridge, Massachusetts 02139; email: tuller@mit.edu

[3]Department of Nuclear Science and Engineering, Massachusetts Institute of Technology, Cambridge, Massachusetts 02139; email: dmarrocc@mit.edu

[4]School of Chemistry, Trinity College Dublin, Dublin 2, Ireland

[5]Department of Energy Conversion and Storage, Technical University of Denmark, Frederiksborgvej, 4000 Roskilde, Denmark; email: ccha@dtu.dk, momo@dtu.dk

[6]University of Maryland Energy Research Center, University of Maryland, College Park, Maryland 20742; email: ewach@umd.edu

Annu. Rev. Mater. Res. 2014. 44:205–39

First published online as a Review in Advance on February 24, 2014

The *Annual Review of Materials Research* is online at matsci.annualreviews.org

This article's doi: 10.1146/annurev-matsci-070813-113329

Copyright © 2014 by Annual Reviews. All rights reserved

*These authors contributed equally to this manuscript.

§Corresponding author.

Keywords

solid-oxide fuel cell, battery, hydrogen storage, decrepitation, exfoliation, mechanical properties

Abstract

Many energy-related materials rely on the uptake and release of large quantities of ions, for example, Li^+ in batteries, H^+ in hydrogen storage materials, and O^{2-} in solid-oxide fuel cell and related materials. These compositional changes often result in large volumetric dilation of the material, commonly referred to as chemical expansion. This article reviews the current knowledge of chemical expansion and aspires to facilitate and promote future research in this field by providing a taxonomy for its sources, along with recent atomistic insights of its origin, aided by recent computational modeling and an overview of factors impacting chemical expansion. We discuss the implications of chemical expansion for mechanical stability and functionality in the energy applications above, as well as in other oxide-based systems. The use of chemical expansion as a new means to probe other materials properties, as well as its contribution to recently investigated electromechanical coupling, is also highlighted.

1. INTRODUCTION

Polymers swell upon exposure to certain solvents (1), whereas the products of metal oxidation often break away from the metal surface due to the larger volume of the oxide scale (2). Such chemically induced mechanical effects are also observed for materials undergoing less dramatic chemical excursions. In analogy to thermal expansion, chemically induced expansion is often referred to as chemical expansion. For example, lithium insertion in battery electrodes, proton incorporation in hydrogen storage materials, and oxygen release in catalyst supports and solid-oxide fuel cell (SOFC) electrodes lead to chemical expansion. Given the brittle nature of many of these materials, chemical expansion can lead to mechanical instability or failure of devices during operation (see **Figure 1**). Furthermore, bond length changes associated with chemical expansion impact electrochemical (3, 4) as well as mechanical (5–8) properties. Although usually considered a detrimental property for applications, chemical expansion has recently emerged as a means to spatially probe the defect concentration of materials, as well as the kinetics of ion transport across interfaces and in the bulk (9–14).

Anomalously high measured thermal expansions in some solids can now be understood on the basis of superimposed chemical expansion contributions. A prime example is illustrated in **Figure 2**, which shows a large increase in expansion in the fluorite-structured solid solution $Pr_{0.1}Ce_{0.9}O_{2-\delta}$ (PCO) upon heating to above ~500°C in air. Investigators have subsequently demonstrated that PCO begins to release significant amounts of oxygen in this temperature range, resulting in a chemical expansion superimposed on top of the thermal expansion, as shown in **Figure 2** (15, 16). The combined thermal and chemical effect leads to a >200% increase in the expansion coefficient with temperature over the conventional thermal expansion coefficient characteristic of the CeO_2 end member (and PCO below 500°C). Although expansions on the order of 1% are commonly observed for materials like PCO, which readily exchange oxygen with the atmosphere, much greater expansion is often observed in battery and hydrogen storage materials [e.g., ~260% strain for full lithiation of Sn (17)!]. Given the relevance of these materials in various battery and fuel cell applications, models have been developed to predict the stresses occurring during these exchange processes (18–21). In addition to the potential for mechanical failure, interest in studying electromechanical coupling of strain and ionic conductivity (22–30), as well as anomalies in elastic behavior (31), as influenced by chemical expansion, is driving the development of relevant electrochemomechanical models (32–35).

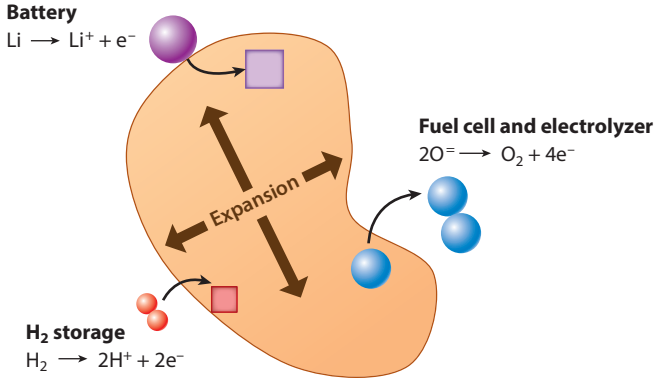

Figure 1

Chemical expansion, associated with gain or loss of ionic species in the solid, can lead to mechanical failure of energy conversion and storage devices.

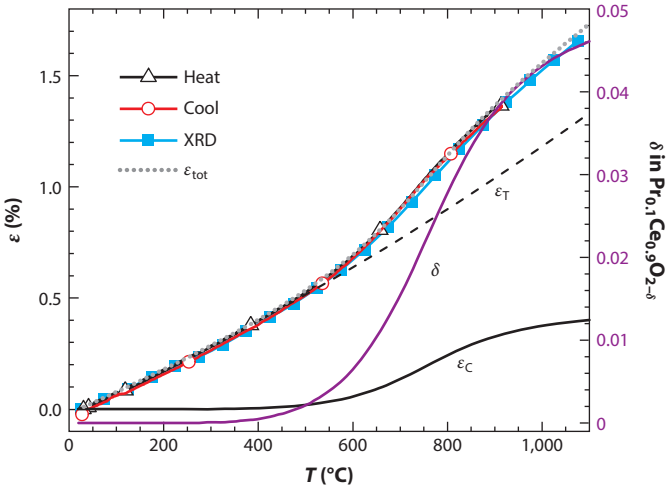

Figure 2

Thermal (ε_T) and chemical (ε_C) expansion of $Pr_{0.1}Ce_{0.9}O_{2-\delta}$. XRD denotes X-ray diffraction. Reprinted with permission from Reference 16.

This review aspires to facilitate and promote future research in this field, in part by providing a taxonomy of different sources of chemical expansion and an overview of chemical expansion in materials groups, with implications for optimized operation of energy conversion and storage devices. First, different forms of chemical expansion, and corresponding coefficients, are introduced and illustrated by examples. We then focus on chemical expansion caused by point defects, termed stoichiometric expansion, and present methods used for measuring chemical expansion. An overview of stoichiometric expansion in different materials groups, and the current state of understanding of its origin and observed trends, follows, placing emphasis on materials associated with solid-oxide electrolyzers and SOFCs. The impact of stoichiometric expansion on mechanical properties of materials, along with a brief discussion of predictive stress modeling for energy conversion and storage devices, is presented. Finally, the use of chemical expansion as a tool to probe other properties is reviewed.

2. FORMS OF CHEMICAL EXPANSION

Chemical expansion is defined as the change in a material's dimensions upon a change in its composition. **Figure 3** schematically shows the types of chemical expansion likely to be observed (also summarized in **Table 1**). Beginning with region 1, the increasing fraction of element B dissolved interstitially in the host lattice A is accompanied by a gradual increase in lattice parameter. With a further increase in B, a composition is reached (region 2), at which point it becomes energetically favorable for the system to form two phases with closely related crystal structures, but with distinct differences in composition (i.e., a miscibility gap) and hence in lattice parameter. Upon passing through this region, one phase (α') is consumed in favor of the other (α''), with a consequent volumetric expansion. Eventually, so much B is accommodated that the second phase (β), with different crystal structure, is precipitated (region 3). The continuous change in lattice parameter with composition (region 1) is referred to as stoichiometric expansion, whereas the abrupt lattice parameter change accompanied by the formation of an additional phase is referred to as phase change expansion. Here the term stoichiometry, defined as "the quantitative relationship between

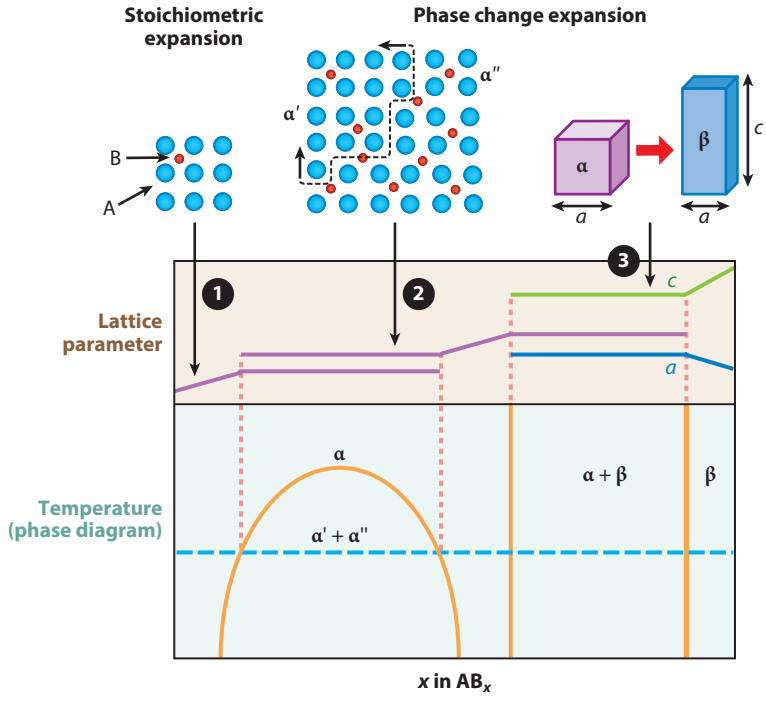

Figure 3

Schematic illustrating stoichiometric and phase change expansion in relation to the dependence of lattice parameter on composition and phase. In this example, α and β are cubic and tetragonal crystal structures, respectively. Region 1 demonstrates the gradual expansion upon a change in composition defined as stoichiometric expansion. Regions 2 and 3 show the larger, discrete increase in lattice parameter associated with a miscibility gap in the former and crystal structure change, defined as phase change expansion, in the latter.

constituents in a chemical substance" (36), is restricted in its meaning to the changes in the ratio of ionic or atomic constituents within a single-phase material. This definition is to be distinguished from stoichiometric phases, in which the ratios of atoms or ions in a compound, such as Al_2O_3 or GaAs, remain in integer values. Indeed, changes in stoichiometry, i.e., deviations from the stoichiometric integer ratios, known as nonstoichiometry, and the corresponding introduction of defects into the lattice, lead to the observed dimensional changes as defined by stoichiometric expansion.

As the examples discussed below make evident, regions 1–3 are commonly observed in batteries, regions 1 and 2 in hydrogen storage materials, and regions 1 and 3 in SOFC and related materials.

Table 1 Definition of different types of chemical expansion (chemically induced expansion)

Chemical expansion: compositionally driven dilation		
Terminology	Phase change expansion	Stoichiometric expansion
Defining characteristics	Dimensional changes associated with a change in crystal structure and/or with a large, discrete change in lattice parameter	Gradual dimensional change with gradual stoichiometry change (no significant crystal structure change)
Examples	Li_xSn, $LaNi_5H_\delta$, Ni/NiO	See **Table 3**

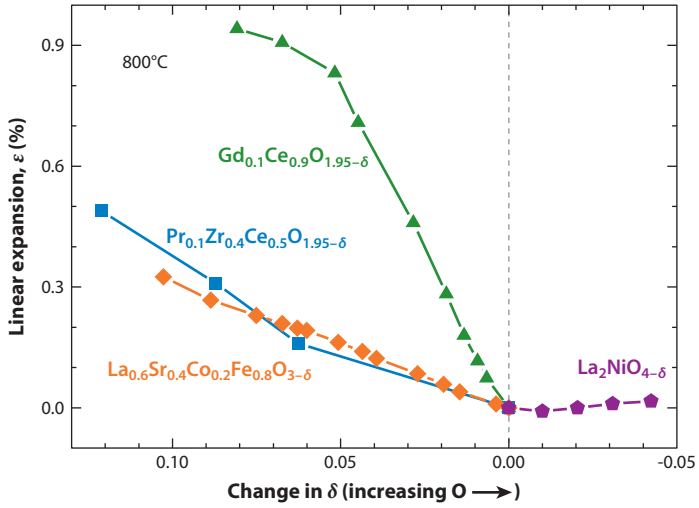

Figure 4

Stoichiometric expansion of selected oxides with change in oxygen content, demonstrating, in contrast to **Figure 3**, shrinkage upon ion incorporation. In a departure from convention, the *x*-axis is plotted in reverse here to facilitate comparison with **Figure 3**. Data were replotted from References 55, 95, 151, and 152.

Whereas batteries and hydrogen storage materials typically, and intuitively, display volumetric expansion upon, for example, lithium and hydrogen insertion, SOFC materials exhibit significant shrinkage with increasing oxygen content, as shown in **Figure 4**. Chemical expansion presents a rich field of study with technological relevance, and our goal in this review is not to cover every example of chemical expansion but instead to highlight key examples. The remainder of this section provides a brief historical perspective of chemical expansion, followed by its impact on selected energy-related technologies.

2.1. Historical Perspectives

As early as the 1950s, several studies were carried out on the effect of gradual reduction (increasing δ) of fluorite-structured oxides like $PrO_{2-\delta}$, $TbO_{2-\delta}$, $ThO_{2-\delta}$, and in particular $CeO_{2-\delta}$ (reduced from CeO_2; $1.7 < \delta < 2$) on the lattice parameter (37, 38). Such studies observed an expansion on reduction, with a linear relationship between the lattice parameter and δ (**Figure 5**). Remarkably, an expansion was seen on reduction, in contrast to the contractions typically observed in solid-state chemistry. Furthermore, the cubic structure was retained over the linear range, which extended to $\delta \sim 0.2$ ($n \sim 1.8$ in **Figure 5**).

Researchers realized that this behavior was a result of reduction of Ce^{4+} to Ce^{3+} and the incorporation of oxide ion vacancies. Many researchers have since attempted to understand this phenomenon. For example, Manes et al. (39) proposed a model of the substoichiometric fluorite-structured compounds on the basis of a new defect, termed the tetrahedral defect and defined as an oxygen vacancy bound to two reduced cations in its coordination tetrahedron. There has been debate about the effective size of oxygen vacancies and their corresponding impact on stoichiometric expansion. The experimental works of Kim (40) and Hong & Virkar (41) along with more recent computational studies (42–44) clearly showed that the effective volume of a vacancy is smaller than that of an oxide ion. Thus, the larger volume of Ce^{3+} compared with that of Ce^{4+} is the only reason for the stoichiometric expansion, as discussed in more detail below in Section 5.

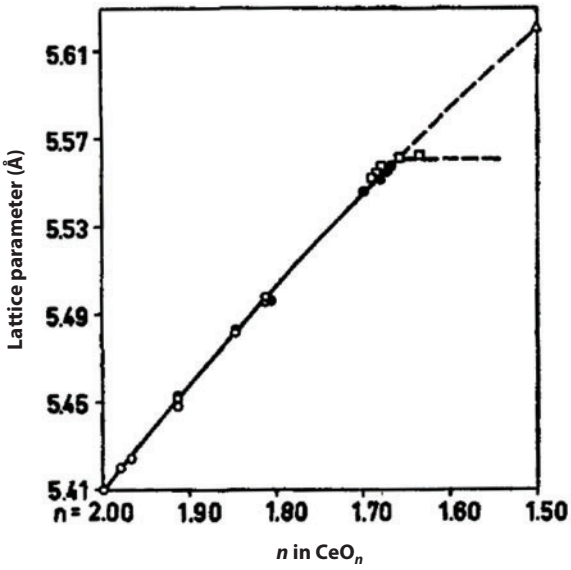

Figure 5

Lattice parameter of cubic ceria with decreasing oxygen content ($n = 2 - \delta$; cf. **Figure 4**). The lattice parameters were calculated for 20°C from values measured at higher temperatures. Reprinted with permission from Reference 38.

In the simplest case, stoichiometric expansion can be described by a Vegard's law (45) relationship between lattice dimension and the fraction of Ce_2O_3 in a solid solution with CeO_2. Analyzed this way, the Vegard's slope is in the range of 2.4–2.7 $\times$ 10^{-4} nm (mol% $Ce_2O_3)^{-1}$ (46). This range in values is probably related to differences in thermal history of the samples, which in turn is related to the degree of defect clustering (discussed in Section 5). This Vegard's slope is equivalent to a stoichiometric expansion coefficient of ~0.11 mol^{-1}, as defined in Section 3. Additionally, many other oxides are tolerant to significant defect concentrations and thus show similar behavior [e.g., perovskites such as doped $LaCrO_3$ (47) and $LaCoO_3$ (48)], as described below and shown in **Table 3** below.

2.2. Solid-Oxide Electrolyzer and Fuel Cell and Gas Separation Membrane Materials

SOFCs convert chemical energy directly to electricity, thereby overcoming limitations of the Carnot cycle with corresponding gains in efficiency (49, 50). For example, electrical efficiencies as high as 65–75% are expected for combined pressurized SOFC and gas turbines (49, 51). Oxygen (typically from air) dissociates and converts to oxide ions at the cathode and drifts through the solid-oxide electrolyte to the anode, where electrochemical oxidation of the fuel (e.g., H_2, CH_4, NH_3) takes place. SOFCs can also be operated in reverse as solid-oxide electrolyzer cells, thereby converting H_2O and/or CO_2 to H_2 and/or CO (e.g., syngas), which upon further treatment can be processed into liquid fuels (52). The sluggish reaction rates at electrodes, representing a key barrier toward low-temperature operation, are typically improved by the use of mixed ionic electronic conductors (MIECs), i.e., oxides that simultaneously conduct oxide ions and electrons. Additionally, MIEC-based oxygen permeation membranes (OPMs) offer a simplified and more cost-effective alternative to electrical pumping of oxygen, as they do not require an external

circuit while maintaining nearly 100% selectivity. As the oxygen content of MIECs generally varies considerably with oxygen partial pressure (P_{O_2}) and temperature (see Section 3), significant stoichiometric expansion occurs, resulting in mechanical stresses, with potentially catastrophic results, as discussed in detail in Section 7.

For example, doped $CeO_{2-\delta}$, which is an MIEC under the conditions prevailing at the fuel side of an SOFC, correspondingly undergoes large stoichiometric expansion, leading in some cases to mechanical failure of ceria-supported cells (53, 54). **Figures 4** and **5** show the stoichiometric expansion of some ceria-based materials (with fluorite structure) upon loss of oxygen (with corresponding formation of oxygen vacancies). Similar behavior is observed for $(La,Sr)(Co,Fe)O_{3-\delta}$, a perovskite-structured MIEC commonly used as the SOFC oxygen electrode (cathode), but with a smaller dependence on δ. In contrast, the formation of oxygen interstitials in the layer-structured $La_2NiO_{4+\delta}$ results in expansion of the *c*-axis and in contraction of the *a*-axis, with negligible overall stoichiometric expansion. The stoichiometric expansion behavior of these three structurally different materials groups, often used in SOFCs, is discussed in greater detail in Section 5. Many other MIEC materials show stoichiometric expansion, and their compositions are summarized in tables of past research publications and reviews as well as in **Table 3** below (20, 47, 55, 56).

Although the above cases focus on oxide ion conductors, certain oxides, such as acceptor-doped $(Ba,Sr)(Zr,Ce)O_{3-\delta}$, accommodate a significant number of protons upon hydration, giving rise to substantial proton conductivity. These classes of materials are investigated as potential electrolytes in proton-conducting fuel cells and for hydrogen separation membranes. Stoichiometric expansion upon proton incorporation in these materials has also been observed (57, 58). For example, Kreuer (57) reported an expansion of 0.4% upon hydration of $BaZr_{0.85}Y_{0.15}O_{3-\delta}$.

As an example of phase change expansion, we turn to Ni/NiO, which, due to its excellent processability and chemical compatibility with the yttria-stabilized zirconia (YSZ) oxygen electrolyte in SOFCs, is often used as the electronically conducting phase in SOFC anodes. However, during high-current operation or shutdown in insufficiently reducing conditions, the oxygen activity can become large enough to oxidize Ni to NiO, resulting in significant phase change expansion and thus often leading to cracking in the SOFC (56, 59). Largely due to the mechanically unforgiving nature of these composite ceramic devices, materials that exhibit phase change expansion are avoided when possible. As a result, most MIECs studied in this field and discussed in this review exhibit relatively smaller stoichiometric expansion within their operational range.

2.3. Battery Materials

Batteries, which reversibly convert electricity to chemically stored energy, provide power to portable devices and electric vehicles as well as backup power for stationary applications. Larger-scale applications, such as load-leveling devices as part of the smart grid, are also being considered (60). Lithium-based batteries offer some of the highest power and energy densities (61). During use of such batteries, the small size of the lithium ion aids in its removal from the solid-state cathode lattice and in its consequent insertion into the corresponding solid-state anode lattice. Both the removal and the insertion of lithium result in significant volume changes of battery electrodes, often referred to as lithium-induced volume change. Woodford et al. (19) summarized measured chemical expansion values for materials used in both lithium- and sodium-based batteries. Although there is considerable spread in these values, sodium generally exhibits a larger expansion than does lithium, in agreement with the larger ionic radius of sodium (62).

Figure 6 shows the chemical expansion measured upon lithium insertion into $Li_xMn_2O_4$ (63). As lithium is initially inserted, the lattice parameter shows a step increase in accord with phase change expansion, although the material remains isostructural. For $x > 0.7$, the lattice parameter

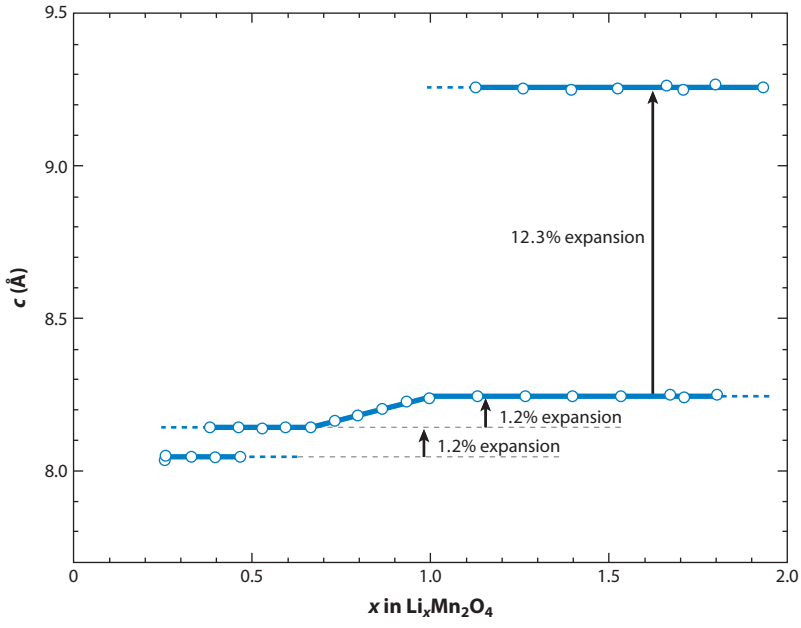

Figure 6

Cubic or pseudocubic lattice parameter upon lithium insertion showing an initial phase change expansion, then stoichiometric expansion, and ultimately a much larger phase change expansion. Reproduced from Reference 63 with permission from The Electrochemical Society.

gradually increases with lithium insertion, thus exhibiting stoichiometric expansion. At $x > 1$, phase change expansion is again observed and is accompanied by a change from a cubic structure to a tetragonal structure.

The 260% volumetric expansion upon lithiation of Sn to Li_4Sn, accompanied by multiple phase changes, is another, more extreme example of phase change expansion (17, 64). In contrast, pure graphite exhibits a 12.8% stoichiometric expansion to LiC_6, accommodating relatively large amounts of lithium by its insertion between hexagonal close-packed layers with no significant change in structure (65). Many other metals readily insert into graphite, with expansion between layers roughly correlated with cation Shannon radius (66, 67). Other lithium battery materials show nearly zero [$Li_x[Li_{1/3}Ti_{5/3}]O_4$; $x \sim 0$–1 (68)] or negative [Li_xCoO_2; $x \sim 0.4$–1 (69)] volumetric chemical expansion. Additionally, hydride formation in nickel metal hydride (NiMH) batteries (70) leads to chemical expansion, as discussed in the next section.

During phase change expansion, upon discharge or charge, the large structural and/or lattice parameter difference between the two phases leads to significant stress buildup, often resulting in cracking, if certain design criteria are not met (19, 71). In lithium batteries, cracking leads to the effective loss of lithium by electrical isolation of lithium-containing particles and to the formation of new surfaces that quickly form an inert, lithium-containing solid-electrolyte interphase (72). Additionally, stress impacts the rate of intercalation and deintercalation in $LiFePO_4$ electrodes (73, 74).

2.4. Hydrogen Storage Materials

Research on hydrogen storage materials is being pursued in part as a strategic component in the hydrogen economy, in which renewably produced hydrogen would replace fossil fuels, in

addition to its current use in NiMH batteries (70). Such materials also play a role as functional materials, for example, in optical switching mirrors, in which the hydride phase is transparent and the metal phase reflective (75, 76). In these materials, hydrogen typically enters the lattice by filling tetrahedral or octahedral sites, forming a solid solution with the metal (α-phase). Once the solubility limit is exceeded, a second, largely isostructural phase (β-phase) is formed with typical volumetric expansions of 10–20% (70). For example, $LaNi_5$ exhibits stoichiometry expansion for small hydrogen content, eventually reaching a miscibility gap with a resultant large 21.5% volume change (i.e., phase change expansion) (77). The phase change can be mitigated by adding copper, resulting in volumetric expansion on the order of 8.5%, but with only approximately half the hydrogen absorption capacity versus that without copper (maximum ~3.2 hydrogen atoms per $LaNi_5Cu$) (78).

As in the case for lithium batteries, this large increase in expansion results in fracturing of the storage material, commonly referred to as decrepitation. Decrepitation increases reaction surface area, improving storage kinetics. However, decrepitation can hinder the required heat transfer upon hydrogen storage and release (due to an increased number of interfaces), reduce gas transport through the more densely packed powder, and potentially deform the container with cycling and migration of powder into undesirable places (e.g., valve seats) (79). Because most hydrogen storage materials are metals and are thus susceptible to plastic deformation, large stresses resulting from inhomogeneous hydrogen absorption (e.g., between α- and β- phases) can contribute to dislocation formation, resulting in chemically driven strain hardening (80). This effect can be substantial in thin films, in which significant twinning and dislocation formation and/or delamination and buckling of the constrained films occur (75, 76). From a thermodynamic viewpoint, the atomic-level expansion occurring around hydrogen atoms is postulated to attract other hydrogen atoms, with a consequent increase in the magnitude of enthalpy for absorption (81, 82). This increased driving force for hydrogen absorption has also been observed for tensile strained films, with the opposite trend in compressively strained films (83). A decrease in the magnitude of lattice expansion upon hydrogenation is observed for tensile strained films, likely due to their larger initial volume.

On a side note, decrepitation originally referred to breaking apart minerals (84) accompanied by a crackling sound. During chemical expansion in batteries, hydrogen storage materials, and SOFCs, acoustic recording of cracking was used to identify the onset of mechanical failure (19, 85, 86).

2.5. Other Applications

Catalyst systems for controlling automotive emissions often employ a support that readily absorbs or releases oxygen to aid in oxidation of unburned hydrocarbons and in the removal of oxygen from NO_x during the typical cycling from a fuel-rich state to a fuel-lean state (87, 88). For example, ceria-zirconia solid solutions are commonly used as oxygen storage materials due to their high redox activity as well as their more modest stoichiometric expansion compared with the larger phase change expansion from, e.g., Cu/CuO, resulting in a lower degree of chemical expansion–induced degradation in the former (87).

Although ion transport is a critical component of the above applications, relatively immobile ionic defects, and the corresponding lattice relaxation around them, in many electroceramics impact device performance. For example, in superconductors, excessive quantities of oxygen vacancies introduced during sample preparation result in an orthorhombic-to-tetragonal phase transition of the perovskite structure, with consequent loss of superconductivity (89–91).

As discussed in Section 1, phase change expansion due to corrosion, for example, rust, presents a significant challenge to industry, in which materials that develop passive, stable coatings (e.g.,

stainless steel) have been intensively researched and developed (2). In concrete materials, internal swelling reactions, commonly associated with hydration of inorganic constituents, occur, resulting in chemical expansion (92).

3. STOICHIOMETRIC EXPANSION COEFFICIENT AND POINT DEFECT MODELING

3.1. Stoichiometric Expansion Coefficient

As discussed above, stoichiometric chemical expansion refers to the change in a material's dimensions upon a change in its chemical composition, or stoichiometry, while being restricted to a single phase. In analogy to the thermal expansion coefficient, the stoichiometric expansion coefficient (α_C), often simply referred to as the chemical expansion coefficient, is defined by (44, 46, 47, 93)

$$\varepsilon = \alpha_C[i], \qquad 1.$$

where the induced strain, ε, is correlated with the concentration of defects $[i]$ responsible for the expansion. In most cases, researchers define $[i]$ in terms of the molar fraction of the corresponding defect responsible for expansion. For example, in $CeO_{2-\delta}$, δ is typically used, as can be seen in **Figures 4** and **5** (where $2 - n = \delta$ in the latter). Although δ is proportional to the concentration of defects, the relationship depends on the chemical formula of the compound. To compare between different chemical formulas (i.e., perovskites versus fluorites), a convention using fractional concentration is more useful. When $[i]$ is listed by using this ratio of oxygen defects to total oxygen in the stoichiometric compound, $[V_O^{\bullet\bullet}] \propto \delta/2$ or $\delta/3$, and $\left[V_O^{\bullet\bullet}\right]$ or $\lfloor O''_i \rfloor \propto \delta/4$ for $MO_{2-\delta}$, $ABO_{3-\delta}$, and $A_2BO_{4+\delta}$ compounds, respectively (196). As is discussed below, stoichiometric expansion arises from simultaneous contributions both from a change in the ionic radii of cations as well as from relaxation around oxygen vacancies and/or interstitials, and therefore one can choose either cation or oxygen defects for i. Throughout this article, we use oxygen vacancies for i. For a listing of α_C values reported for SOFC-related materials, see **Table 3** and **Figure 8** (below). A similar table for battery-related materials can be found in Reference 19.

3.2. Point Defect Modeling

As discussed above, chemical expansion results from lattice parameter changes induced by changes in the chemical composition of a solid. These changes can be induced by chemical or electrochemical exchange of cationic or anionic species between the solid of interest and adjacent gas, liquid, or solid phases. The manner in which these chemical composition changes are accommodated can differ considerably between different solids. For example, oxygen loss induced by exposing metal oxides to reducing conditions can result in the creation of either oxygen vacancies, as in $CeO_{2-\delta}$ (94, 95), or metal interstitials, as in $Zn_{1+\delta}O$ (96). The associated change in oxidation state of the material is normally accommodated by a change in oxidation state of a subset of the cations, e.g., Ce^{4+} to Ce^{3+} in the former case and Zn^{2+} to Zn^{1+} in the latter. Such cations can be further subcategorized by whether the extra electrons are localized, as in the ceria case, or delocalized within the conduction or valence band, as in the case of ZnO. Defect chemical models (which describe how composition changes are accommodated in the crystal lattice of a given solid, under thermodynamic equilibrium conditions, as the temperature and the chemical environment of the solid are varied) allow for predictions of key properties, including diffusivity (97), electrical conductivity (98, 99), mass change (100), and (of particular relevance to this article) chemical expansion. For a

detailed discussion of defect equilibria in oxides, we direct the reader to a previous *Annual Review of Materials Research* article by two of the authors (32). In the following, we present a brief summary, emphasizing concepts of direct relevance to this discussion of chemical expansion.

We begin by describing the defect equilibria in $Pr_xCe_{1-x}O_{2-\delta}$, the solid solution of praseodymia and ceria, whose thermal expansion (ε_T) and chemical expansion (ε_C) are illustrated in **Figure 2**. Upon heating, these fluorite-structured solid solutions lose oxygen by the formation of oxygen vacancies and by the simultaneous reduction of Pr^{4+} to Pr^{3+} (15, 101). This reduction reaction can be described by

$$2\,Pr_{Ce}^{\times} + O_O^{\times} \leftrightarrow V_O^{\bullet\bullet} + 2\,Pr_{Ce}^{/} + 1/2O_2(g). \quad 2.$$

Here, $Pr_{Ce}^{\times}$ and $Pr_{Ce}^{/}$ represent praseodymium substituting on a cerium site with 4+ and 3+ valences, respectively; $O_O^{\times}$, an oxide ion on a normal oxygen site; and $V_O^{\bullet\bullet}$, an oxygen vacancy with a net 2+ charge relative to the normal lattice charge. The corresponding mass action relationship is given by

$$\frac{[Pr_{Ce}^{/}]^2[V_O^{\bullet\bullet}]P_{O_2}^{1/2}}{[Pr_{Ce}^{\times}]^2[O_O^{\times}]} = K_{r,Pr}^{\circ}\exp\left(-\frac{H_{r,Pr}}{kT}\right) = K_{r,Pr}. \quad 3.$$

Here, the brackets denote concentration; P_{O_2} is oxygen partial pressure; and the right-hand side of the equation is the mass action constant characterized by the reduction enthalpy, $H_{r,Pr}$, as expressed in the exponent. The mass and site conversion relationships are given by

$$[Pr_{Ce}^{/}] + [Pr_{Ce}^{\times}] = [Pr_{Ce}]_{total} = x[Pr_x\,Ce_{1-x}O_{2-\delta}]. \quad 4.$$

and

$$[V_O^{\bullet\bullet}] + [O_O^{\times}] = 2\,[Pr_x\,Ce_{1-x}O_{2-\delta}]\,, \quad 5.$$

respectively. Here, $[Pr_x\,Ce_{1-x}O_{2-\delta}]$ is the concentration of PCO expressed per cubic centimeter, and the level of nonstoichiometry is given by

$$\delta = [V_O^{\bullet\bullet}]/[Pr_x\,Ce_{1-x}O_{2-\delta}]. \quad 6.$$

In high-P_{O_2} conditions (e.g., in air), in which cerium remains largely tetravalent (as opposed to the example shown in **Figure 5** under highly reducing conditions), the electroneutrality equation can be approximated by (101)

$$[Pr_{Ce}^{/}] \cong 2[V_O^{\bullet\bullet}]. \quad 7.$$

One can easily solve for the two key defect species, $Pr_{Ce}^{/}$ and $V_O^{\bullet\bullet}$, that contribute to chemical expansion by simplifying Equation 4 on the basis of the operating conditions. For example, at sufficiently high P_{O_2}, $[Pr_{Ce}^{\times}] \approx [Pr_{Ce}]_{total}$, which, together with Equation 7, can be substituted into Equation 3 to give

$$[Pr_{Ce}^{/}] = 2[V_O^{\bullet\bullet}] = 2^{1/3}[Pr_{Ce}]_{total}^{2/3}[O_O^{\times}]^{1/3}K_{r,Pr}(T)^{1/3}P_{O_2}^{-1/6}. \quad 8.$$

As a consequence, both $[Pr_{Ce}]$ and $[V_O^{\bullet\bullet}]$, or equivalently δ, can be predicted as functions of T, P_{O_2}, and praseodymium concentration, and likewise, the chemical expansion, which depends on both of these defects, can be predicted as discussed below.

We now turn our attention to chemical expansion in batteries and discuss the electrochemical injection and extraction of lithium ions from lithium battery electrodes during charge/discharge cycles. Lithium battery cathodes based on the $LiFePO_4/FePO_4$ system are attractive given that the abundant transition metal iron would be expected to accommodate changes in lithium stoichiometry by a change in its valence state from 3+ to 2+ and, as such, is a beneficial alternative to the more expensive cobalt or nickel cations (102). As we see below, this expectation is not completely fulfilled. Whereas $LiFePO_4$ exhibits lithium deficiency ($Li_{1-y}FePO_4$ for $y \leq 0.05$), $FePO_4$

accommodates lithium excess (Li_xFePO_4 for $x \leq 0.17$). An attractive feature of this system as a battery cathode is the voltage plateau for lithium contents between 0.17 and 0.95. This plateau is due to a so-called two-phase mechanism (103), which corresponds to region 2 of **Figure 3**, in which both phases coexist and the lithiation process proceeds with one phase being consumed at the expense of the other.

The defect chemical investigation of the Li_xFePO_4 phase by Zhu et al. (104) is instructive. Here one can describe the insertion of lithium into this phase by

$$\mathrm{Li(s)} + \mathrm{V}_i^{\times} \leftrightarrow \mathrm{Li}_i^{\bullet} + e^{/}, \qquad 9.$$

in which lithium enters an empty interstitial site and gives up its electron to the conduction band, which one might assume is of iron 3*d* character. Although this reaction assumes full ionization of lithium interstitials, experimental evidence suggests otherwise. Instead, one needs to include the ionization reaction and the corresponding mass action relation given by

$$\mathrm{Li}_i^{\bullet} + e^{/} \leftrightarrow \mathrm{Li}_i^{\times}, \qquad 10.$$

$$\frac{[\mathrm{Li}_i^{\times}]}{[\mathrm{Li}_i^{\bullet}][e^{/}]} = K(T) = K_o \exp\left(-\frac{E_{\mathrm{ionization}}}{kT}\right), \qquad 11.$$

in which Zhu et al. (104) estimated an ionization energy, $E_{\mathrm{ionization}}$, of ~1 eV. Thus, in estimating chemical expansion in Li_xFePO_4, given the small fraction of inserted lithium ions that ionize to give up their electrons, one need consider largely the impact of the excess lithium, without measureable influence of the iron valence change from 3+ to 2+ in this phase. Indeed, the low degree of ionization of the lithium is consistent with the highly resistive nature of this electrode even after substantial lithiation (102).

4. MEASUREMENT OF CHEMICAL EXPANSION

Experimental determination of the chemical expansion coefficient requires measurements of two properties: isothermal uniaxial strain and isothermal change in stoichiometry (relative to a reference point). Typically, each property is monitored over a range of imposed activities of a constituent element, e.g., by changing oxygen, hydrogen, or water partial pressures or by varying the degree of lithium or sodium insertion; such measurements are tracked over time to ensure equilibration of the sample in each condition. Strain and stoichiometry measurements may be conducted simultaneously, as in the case of, e.g., neutron diffraction, or separately in identical conditions, e.g., by dilatometry and thermogravimetric analysis over the same P_{O_2} and temperature range. **Figure 7** shows an example of measured strain over time, in response to changes in P_{O_2} (93). Combining the equilibrated values from this result with the measured equilibrium stoichiometry change at the corresponding P_{O_2} values results in a plot of expansion versus change in nonstoichiometry like the plot shown in **Figure 4**, in which the slope is the chemical expansion coefficient (see Equation 1).

As summarized in **Table 2**, techniques applied to measure strain can be divided into those that study atomic-scale structure changes [e.g., neutron diffraction, X-ray diffraction (XRD), electron diffraction, transmission electron microscopy, and scanning probe microscopy] and those that measure macroscopic size changes (e.g., dilatometry, interferometry, digital image correlation, and bilayer curvature). Techniques applied to measure changes in stoichiometry include measurements of crystal structure (neutron diffraction), mass change (thermogravimetric analysis), electrical response (coulometric titration, chemical capacitance measurements), and optical properties (thin-film optical absorption or bulk, diffuse reflectance measurements). The limitations listed for each

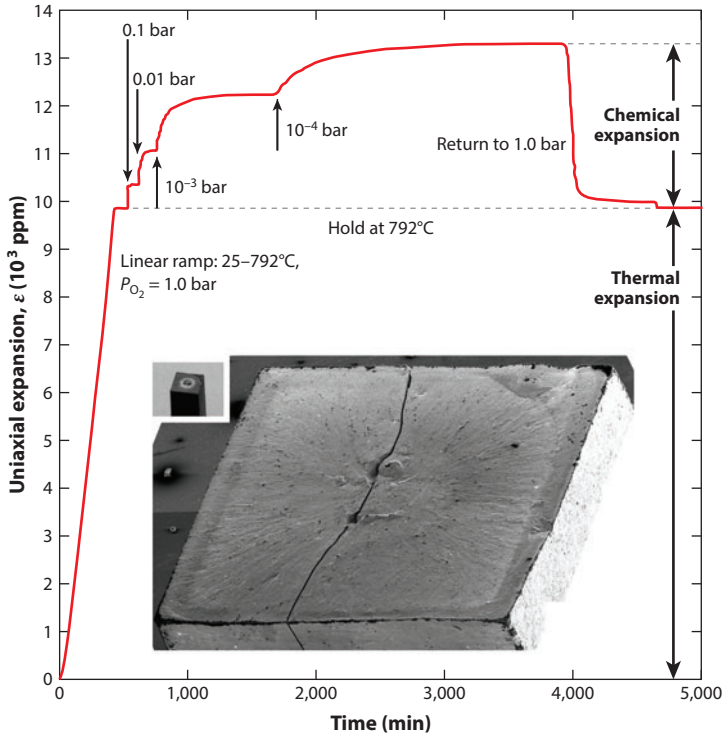

Figure 7

Thermal and chemical expansion measured by using dilatometry on a dense $La_{0.6}Sr_{0.4}Co_{0.2}Fe_{0.8}O_{3-\delta}$ bar. At the end of the measurement, some chemical expansion–induced cracking is observed on the end of the bar, as shown in the image inset. Reprinted with permission from Reference 93.

technique may help guide which measurement is appropriate for a given sample; for example, an approach may be more appropriate for bulk versus thin-film samples or for large versus small samples.

5. TRENDS AND ORIGIN OF THE STOICHIOMETRIC EXPANSION COEFFICIENT

This section discusses trends observed for α_C for three classes of materials (fluorite, perovskite, and Ruddlesden-Popper structures) used in SOFCs. The existing empirical models and recent simulation work used to uncover the origin of stoichiometric expansion are then described. Finally, other factors that can contribute to chemical expansion, such as defect interactions, are briefly reviewed.

5.1. Trends

Table 3 lists a representative selection of α_C values for different nonstoichiometric oxides, belonging to three structurally different materials groups: fluorite-type, doped $CeO_{2-\delta}$; perovskites; and K_2NiF_4 layered oxides. Most data in **Table 3** are based on dilatometry measurements, which, due to reliable thermal equilibrium and sub-part-per-million length resolution, are generally believed to be highly accurate. These values, and values reported throughout the text, are calculated with respect to δ, following convention. In contrast, **Figure 8** shows a graphical representation of α_C

Table 2 Selected experimental techniques for measurement of isothermal expansion and stoichiometry changes required for determination of chemical expansion

Technique	Properties measured	Limitations	References
Neutron diffraction	Lattice parameters, stoichiometry	Large sample size, powders, crystalline	126, 153–156
X-ray diffraction	Lattice parameters, stoichiometry in some cases	Crystalline samples, potential for nonuniform temperature in conditions of elevated temperature	58, 109, 157, 158
Dilatometry	Length	Large bulk samples, no irreversible length changes (e.g., from sintering during measurement)	48, 126, 159–161
Interferometry	Length or thickness change	Usually bulk or thin-film flat samples; other samples possible	162–165
Digital image correlation	Strain	Large expansions required	166
Bilayer curvature	Stress and strain via curvature	Bilayers with elastically deforming substrate	167–169
Scanning probe microscopy	Surface position (height)	Limited sample size, temperature and gas pressure limits	11, 170–173
Thermogravimetric analysis	Stoichiometry change	Large sample size; corrections for buoyancy effects required	95, 174–178
Coulometric titration	Stoichiometry	Bulk or thin film	179–182
Chemical capacitance	Changes in stoichiometry with respect to changes in electrochemical potential	Useful for thin films; stray/interfacial capacitances must be derived/isolated	183–186
Optical absorption	Stoichiometry	Requires optically active defect centers; useful for thin films	187–189
Transmission electron microscopy (sometimes with electron diffraction and/or EELS/EDS[a])	Volume and shape changes, lattice parameters, local stoichiometry (in some cases)	Small sample size, less precision, temperature and gas pressure limits	190, 191

[a]EELS/EDS denotes electron energy loss spectroscopy/energy-dispersive spectroscopy.

on the basis of the fraction of oxygen vacancies. In light of the discussion regarding Equation 1, the oxygen vacancy fraction is likely a better method with which to compare chemical expansion coefficients across different structures, as it is not encumbered by differences in formula units, as in the case of molar fraction (196). Comparing α_C values for different structures in **Table 3** versus **Figure 8**, one can see that apparent differences in α_C are reduced for the oxygen vacancy fraction representation.

Cubic fluorite-structured, acceptor-doped $CeO_{2-\delta}$ MIECs exhibit the highest α_C values and show the largest variation with composition among the three structural classes considered here. The α_C of doped $CeO_{2-\delta}$ tends to increase with increasing levels of trivalent doping (105) and dopant ionic radius (15), consistent with initially longer bond lengths and hence reduced bond strength. However, α_C is often found to be independent of temperature (16) and oxygen stoichiometry (105, 106).

Perovskites possess consistently lower α_C values than do fluorites, as first noted by Atkinson & Ramos (20), who wrote that "the chemical expansion per oxygen vacancy in the perovskite structure is intrinsically lower than in the fluorite structure." Most of these materials have a cubic or pseudocubic structure, although recent experiments by Grande and colleagues (107–110) showed

Table 3 Stoichiometric expansion values based on δ; see Equation 1[a]

Material	δ range	T (°C)	α_C	Reference(s)
Fluorite-ceria				
$CeO_{2-\delta}$	0–0.1	800–900	0.10	106
$CeO_{2-\delta}$	0–0.105	900	0.11	105
$CeO_{2-\delta}$	0–0.2	900	0.11	105
$Gd_{0.1}Ce_{0.9}O_{1.95-\delta}$	0–0.07	800	0.13	138
$Gd_{0.18}Ce_{0.82}O_{1.91-\delta}$	0–0.06	900	0.13	105
$Gd_{0.4}Ce_{0.6}O_{1.8-\delta}$	0–0.045	900	0.15	105
$Pr_{0.2}Ce_{0.8}O_{2-\delta}$	0.1–0.14	800	0.11	15
$Pr_{0.15}Tb_{0.05}Ce_{0.8}O_{2-\delta}$	0.1–0.14	800	0.105	15
$Pr_{0.05}Tb_{0.15}Ce_{0.8}O_{2-\delta}$	0.1–0.14	800	0.095	15
$Tb_{0.2}Ce_{0.8}O_{2-\delta}$	0.1–0.14	800	0.09	15
$Tb_{0.2}Ce_{0.8}O_{2-\delta}$	0.05–0.1	800	0.09	15
$Pr_{0.1}Tb_{0.1}Ce_{0.8}O_{2-\delta}$	0.05–0.1	800	0.07	15
$Pr_{0.2}Ce_{0.8}O_{2-\delta}$	0.05–0.1	800	0.085	15
$Pr_{0.1}Ce_{0.9}O_{2-\delta}$	0.008–0.05	650	0.087	16
$Pr_{0.1}Ce_{0.9}O_{2-\delta}$	0.033–0.056	900	0.087	16
$Pr_{0.1}Zr_{0.4}Ce_{0.5}O_{1.95-\delta}$	0–0.14	700–900	0.046	152
Perovskite				
$La_{0.8}Sr_{0.2}CoO_{3-\delta}$	0.015–0.09	891	0.027	48
$La_{0.6}Sr_{0.4}CoO_{3-\delta}$	0.105–0.225	892	0.033	48
$La_{0.3}Sr_{0.7}CoO_{3-\delta}$	0.24–0.36	901	0.04	48
$La_{0.6}Sr_{0.4}Co_{0.8}Fe_{0.2}O_{3-\delta}$		800	0.022	140
$La_{0.6}Sr_{0.4}Co_{0.2}Fe_{0.8}O_{3-\delta}$	0.05	700–890	0.032	93
$La_{0.6}Sr_{0.4}Co_{0.2}Fe_{0.8}O_{3-\delta}$	0.03–0.12	800	0.036	192
$La_{0.3}Sr_{0.7}FeO_{3-\delta}$	0.09–0.24 0.16–0.32	650 900	0.017 0.047	160
$La_{0.3}Sr_{0.7}Fe_{0.6}Ga_{0.4}O_{3-\delta}$	0.25–0.33 0.29–0.34	650 900	0.021 0.06	160
$La_{0.7}Sr_{0.3}CrO_{3-\delta}$	0–0.12	1,000	0.023	193
$La_{0.7}Ca_{0.3}CrO_{3-\delta}$	0.02–0.12	1,000	0.036	193
$La_{1-x}Sr_xCrO_{3-\delta}$ (x = 0.16–0.3)		1,000	0.024	47
$La_{0.9}Sr_{0.1}Cr_{0.87}Mg_{0.10}V_{0.03}O_3$	0–0.05	1,000	0.023	194
$La_{0.8}Sr_{0.2}Cr_{0.97}V_{0.03}O_3$	0–0.07	1,000	0.03	194
$La_{0.8}Sr_{0.2}Cr_{0.87}Fe_{0.10}V_{0.03}O_3$	0–0.08	1,000	0.03	194
$LaMnO_{3-\delta}$	0–0.04	600–1,000	0.024	195
$Ba_{0.6}Sr_{0.4}Co_{0.8}Fe_{0.2}O_{3-\delta}$		600–900	0.026–0.016	153
K_2NiF_4				
$La_2NiO_{4-\delta}$	−0.1 to −0.06	800	0.002 0.028 (//*a*) −0.076 (//*c*)	124
$La_2Ni_{0.9}Fe_{0.1}O_{4-\delta}$	−0.11 to −0.08	800	0	124
$La_2Ni_{0.9}Co_{0.1}O_{4-\delta}$	−0.12 to −0.09	800	0.006	124
$La_2Ni_{0.8}Cu_{0.2}O_{4-\delta}$	−0.08 to −0.05	800	0.001	124

(*Continued*)

Table 3 (*Continued*)

Material	δ range	*T* (°C)	α_C	Reference(s)
$La_2NiO_{4-\delta}$	−0.1 to −0.05	800	0.004	151
$La_{1.8}Sr_{0.2}NiO_{4-\delta}$	−0.02–0	800	0.002	151
$Nd_2NiO_{4-\delta}$	−0.12 to −0.07	800	−0.002	125
$Nd_{1.8}Sr_{0.2}NiO_{4-\delta}$	−0.05 to −0.01	800	−0.007	125
$La_{1.08}Sr_{0.88}Fe_{0.8}Co_{0.2}O_{4-\delta}$	0–0.09	1,050	0.01	192
$La_{0.98}Sr_{0.98}Fe_{0.8}Co_{0.2}O_{4-\delta}$	0–0.13 0–0.13	1,050 800	0.012 0.02 0.013 (//*a*) 0.033 (//*c*)	126, 192
$La_{0.88}Sr_{1.08}Fe_{0.8}Co_{0.2}O_{4-\delta}$	0.02–0.16	1,050	0.012	192
$Pr_{0.98}Sr_{0.98}Fe_{0.8}Co_{0.2}O_{4-\delta}$	0–0.13	1,050	0.013	192
$La_{1.18}Sr_{0.78}Fe_{0.64}Co_{0.16}Mg_{0.2}O_{4-\delta}$	0–0.12 0–0.13	1,050 1,000	0.011 0.016 0.011 (//*a*) 0.026 (//*c*)	126, 192

[a]See **Figure 8** for a comparison based on site fraction.

that strontium-doped $LaCrO_3$ and $LaMnO_3$ exhibit anisotropic thermal and chemical expansions. The lattice expansion observed in these materials is affected by a wealth of intercorrelated factors, such as subtle crystal structure changes (111–115), transition metal spin states (55, 116–118), cation site (A versus B) (119–122), charge localization/delocalization (43, 123), temperature, and

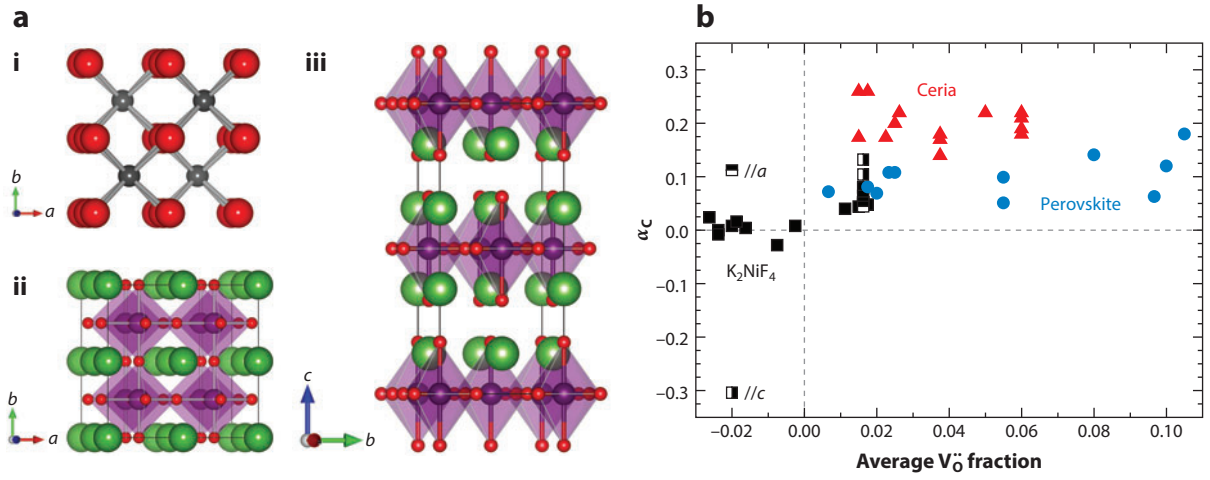

Figure 8

(*a*) Crystal structure of materials with a (*i*) fluorite, (*ii*) perovskite, and (*iii*) K_2NiF_4 layered (Ruddlesden-Popper) structure. Oxide ions are in red, cations in the fluorite structure are in gray, and the big/small cations of the perovskite and Ruddlesden-Popper structure are in green/purple, respectively. (*b*) Stoichiometric expansion coefficient (α_C) calculated with respect to the fraction of oxygen vacancies for a representative selection of fluorite-structured, doped $CeO_{2-\delta}$; perovskites; and Ruddlesden-Popper oxides as a function of the average oxygen vacancy fraction of the measurement range. The negative fraction of oxygen vacancies corresponds to the fraction of oxide ion interstitials relative to oxide ions.

stoichiometry. Such factors make the interpretation of atomistic origins of this expansion difficult, as discussed below.

K_2NiF_4-type layered oxides, in contrast, show the smallest α_C values for studied compositions, even attaining negative values in some cases. The structure (shown in **Figure 8**) consists of perovskite and rock-salt layers parallel to the (*a*,*a*)-plane and alternating along the *c*-direction; all compositions included here adopt the tetragonal *I*4/*mmm* space group for reported α_C values. K_2NiF_4-type oxides can accommodate interstitial oxide ions in the rock-salt layers as well as oxide ion vacancies in the perovskite planes, thereby showing oxygen hyperstoichiometry ($\delta < 0$) or substoichiometry ($\delta > 0$), depending on composition, temperature, and P_{O_2}.

Due to the tetragonal symmetry of the structure, the stoichiometric expansion or contraction is anisotropic, with different α_C values along the *a*- and *c*-directions (124–126). In the superstoichiometric range ($\delta < 0$), a decrease in the concentration of oxide ion interstitials results in expansion along the *a*-axis (//*a*) and in contraction along the *c*-axis (//*c*) (124, 125), as indicated in **Figure 8**. The dimensional changes in the //*a*-directions are dominated by the increase in size of the B-site cations upon reduction (124). In contrast, the contraction in the //*c*-direction is related to the loss of electrostatic repulsion between oxide ion interstitials in the rock-salt layers and lattice oxygen in the perovskite layers (124). Although the overall volume change is small, the individual values of α_C //*a* and //*c* are quite significant (124).

In the substoichiometric range ($\delta > 0$), reduction leads to an increase in the concentration of oxide ion vacancies in the perovskite layers, with resultant expansion in both the *a*- and *c*-directions (126). Although the dimensional changes reflect the increasing ionic radii of the B-site cations upon reduction, the two- to three-times-smaller stoichiometric expansion along the *a*-direction compared with that along the *c*-direction indicates a constraining action of the rock-salt layers on the perovskite layers (126). In contrast, the perovskite layers can expand freely along the *c*-direction, thereby yielding pseudocubic α_C values comparable to those of perovskites with related compositions.

5.2. Analytical Models and Empirical Formulas for Chemical Expansion

The prediction of lattice parameters for doped materials has been the subject of intensive study over the past three decades (40, 41, 119–122). As discussed in Section 2.1, numerous studies in the 1980s attempted to introduce a simple relationship between the lattice parameter of a doped MO_2 oxide (mostly CeO_2 or ZrO_2) and the oxide's dopant type and concentration. The first comprehensive study may have been that of Kim (40), who introduced empirical expressions to describe the evolution of the lattice parameters of five fluorite-structured systems (HfO_2, ZrO_2, CeO_2, ThO_2, and UO_2), doped with either divalent or trivalent cations. In this work, Kim performed a multiple regression analysis to correlate changes in lattice constants with microscopic chemical parameters of the constituent ions, such as ionic radii, valence, and electronegativity. Only the first two parameters correlated with lattice parameter, resulting in the following empirical equation for ceria (similar equations for the other compounds can be found in the original paper) (40):

$$a_{Ce} = 0.5413 + \sum_k (0.0220\Delta r_k + 0.00015\Delta z_k)100x_k, \qquad 12.$$

where *a* is the fluorite lattice parameter (in nanometers), Δr_k is the cation radius difference (in nanometers) between the *k*th dopant cation and the host cation ($r_k - r_h$), Δz_k is the valence difference between the *k*th dopant cation and the host cation ($z_k - z_h$), and x_k is the molar

concentration of the kth dopant cation.[1] The authors do not report the range of dopant concentration used in the fitting procedure, but careful reading of the cited literature indicates that the range is 0–25 mol%, with most data points centered at approximately 10 mol% cation concentration. Equation 12 predicts the lattice parameter of doped ceria; deviations between calculated values and experimental values are less than 0.3%.

By setting the derivative with respect to concentration of Equation 12 equal to zero, a critical radius, r_C, i.e., a radius of the dopant that does not result in an increase or a decrease in the lattice parameter, was introduced. This concept is associated with minimized lattice distortions upon doping, leading to maximized oxide ion mobility and, in some cases, inspiring double doping to obtain r_C (28, 40, 41, 127–129). Interestingly, r_C values are larger than the radius of the host cation. For example, r_C of a trivalent cation dopant in ZrO_2 is 0.948 Å, significantly bigger than the radius of zirconium (0.84 Å). As discussed in more detail below, a lattice contraction around vacancies introduced by doping partially compensates for expansion associated with the dopant, thus requiring a larger cation to maintain a constant lattice parameter.

In 1995, Hong & Virkar (41) adopted a hard-sphere structural model to describe the lattice parameters of ceria and zirconia. The key innovative step of their work was to introduce the concept of an oxygen vacancy radius, i.e., treating a vacancy as if it were simply another ionic species with an empirical radius. In the hard-sphere model, the cation-anion bond distance is taken to be the sum of the respective radii, $r_{cation} + r_{anion}$, where r_{cation} and r_{anion} are the cation and anion radii, respectively. The lattice parameter can thus be written as a simple function of r_{cation} and r_{anion}. In the case of the fluorite structure, the lattice parameter reads as follows:

$$a = \frac{4}{\sqrt{3}}(r_{cation} + r_{anion}). \quad 13.$$

In their work, the authors assume that the cation radius is a weighted average of the dopant (r_M) and host (r_{Ce}) cation radii:

$$r_{cation} = xr_M + (1 - x)r_{Ce}. \quad 14.$$

Similarly, the anion radius is a weighted average of the oxide ion (r_O) and vacancy radius (r_V):

$$r_{anion} = \left[\frac{2 - 0.5x}{2}\right] r_O + \left[\frac{0.5x}{2}\right] r_V = [1 - 0.25x]\, r_O + 0.25x r_V. \quad 15.$$

By substituting Equations 14 and 15 into Equation 13, one obtains the expression below for lattice parameter dependence on dopant concentration and ionic radius:

$$\begin{aligned} a(x, r_M) &= \frac{4}{\sqrt{3}} [xr_M + (1 - x)\, r_{Ce} + (1 - 0.25x)\, r_O + 0.25x r_V] \times 0.9971, \\ &= a_0 + \frac{4}{\sqrt{3}} x\, [r_M - r_{Ce} - 0.25r_O + 0.25r_V] \times 0.9971 \quad 16. \end{aligned}$$

where a_0 is the lattice parameter of stoichiometric ceria. The multiplying factor 0.9971 was introduced to compensate for a slightly overestimated a_0 compared with that of experiment.

Equation 16 allows one to predict, using only knowledge of the cation and anion ionic radii (including the vacancy radius), the lattice parameter of CeO_2 doped with any amount of trivalent cation. The latter is an empirical parameter that was determined by fitting to experimental data. The range of studied dopant cation concentrations was 0–22 mol%, with most points centered at

[1] For the sake of consistency, the same nomenclature is used throughout the entire article. For this reason, some of the symbols and equations appear differently than in the original work.

approximately 10 mol%. The estimated vacancy radii, r_V, were 1.164 and 0.993 Å for ceria and zirconia, respectively, and, as discussed above, are smaller than an oxide ion.

These two models have some important limitations. First, both models do not take into account the effects of defect ordering; Vegard's law is actually taken as the starting point. Hong & Virkar (41) briefly discuss this issue and note that their model does not work as well for very high dopant concentrations (>15%, when Vegard's law does not seem to apply) due to defect ordering. Second, in principle, when the fluorite structure is acceptor doped, vacancies are introduced, and the cations attain a coordination number that is lower than 8, which in turn affects their effective ionic radii. This effect in taken into account only indirectly by introducing r_V and fitting its value to experimental data. Furthermore, the constant r_V value does not reflect the varying average coordination number with varying amount of doping. Finally, even though the vacancy radius concept is a way to describe the origin of the contributions to the volume change that are related to change in stoichiometry, it does not add much to the understanding of the local structural modifications taking place in the neighborhood of an oxide ion vacancy. For the last point, we turn to computation modeling, as discussed in the next section.

Fluorite-structured compounds are relatively easy to describe in terms of simple empirical models, such as the ones described above. This is due to the facts that they have a cubic structure (only one lattice parameter to model) and that, when doped with trivalent cations, these compounds form stable, cubic solid solutions over a broad composition range. Materials that crystallize in other structures, such as perovskites, are not so readily modeled, because they usually undergo a series of phase transitions (to noncubic structures) as the temperature and/or dopant cation is changed (119–122). Also, their lattice parameter is affected by other factors such as charge localization and spin state (55, 116). As a consequence, the chemical expansion of some of these materials, for instance, is highly anisotropic (107–110). For this reason, several models (119–122) attempt to relate the lattice parameters to microscopic quantities, such as the ionic radius, valence, electronegativity, and tolerance factor, and the reader is referred to these papers for further discussion.

5.3. Atomistic Origins of Chemical Expansion–Employing Computational Simulations

We recently initiated a more fundamental investigation into the underlying causes of chemical expansion in fluorite-structured materials. Although chemical expansion was experimentally characterized (see **Table 3**) and certain trends were well described by the above-introduced empirical formulas, the atomic-level relaxations associated with chemical expansion were not clear. Ceria was chosen as an ideal model system due to its cubic structure and ability to form extensive solid solutions with trivalent cations. This study was aided by density functional theory (DFT) and classical molecular dynamics (MD) simulations.

Equations 13 and 16 make clear that two chemical reactions are likely responsible for the chemical expansion observed in ceria, namely (*a*) replacing a Ce^{4+} (0.97-Å) cation with a trivalent cation, in this case Ce^{3+} (1.143 Å), and (*b*) replacing an oxide ion with an oxygen vacancy. Here we treat the reduction process as tantamount to doping ceria with Ce^{3+}. This approach is justified by the strongly localized nature of the *f*-electrons observed in this material (43, 131). To separate the effects of cerium cation radius change and oxygen vacancy formation on chemical expansion, MD simulations were performed on a hypothetical system in which the ionic radius of Ce^{3+} was set equal to that of Ce^{4+}. This system was dubbed equal-radius $Ce^{4+}{}_{1-x}Ce^{3+}{}_xO_{2-x/2}$. **Figure 9*a*** reports the calculated lattice parameter versus the vacancy concentration; oxygen vacancy formation by itself, without a cation radius change, results in a contraction of the lattice parameter.

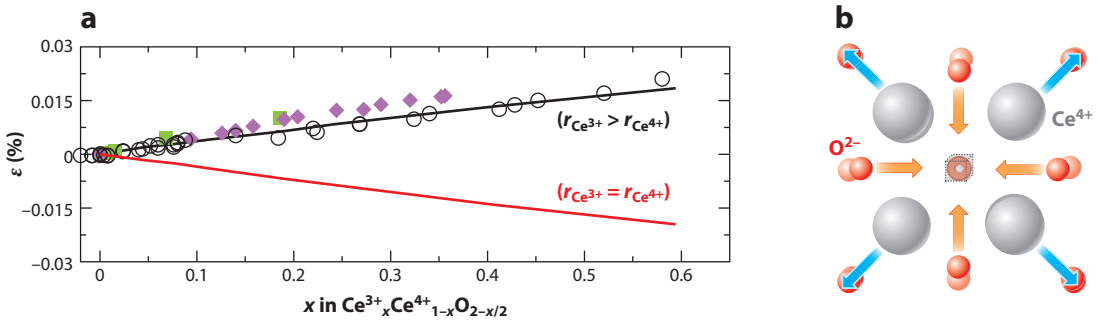

Figure 9

(*a*) Simulated stoichiometric expansion showing the shrinkage (*red line*) when only oxygen vacancies contribute. The simulation (*black line*) shows that, when the increasing radius of cations upon reduction is accounted for, the material expands, in agreement with literature (*points*). (*b*) Cations are repelled from (*blue arrows*), whereas oxide ions are attracted to (*orange arrows*), an oxygen vacancy. Reprinted with permission from Reference 44.

The visualization of the atomic relaxation pattern around a vacancy in **Figure 9*b*** provides a clear explanation of why a vacancy induces a lattice contraction. The removal of an oxide ion causes the neighboring ions to relax significantly. The nearest cations move away from the vacancy by ∼0.10 Å (as consequence of their now-unscreened coulombic repulsion), whereas the nearest oxide ions move toward the vacancy by ∼0.16 Å. Relaxations of ions that are further away from the vacancy also occur, although such relaxations are small and die off with increasing distance (44). At the unit cell level, the total effect of these relaxations is a lattice contraction (see also figure 1 of Reference 132, which clearly depicts this effect), which is described empirically by the vacancy radius. The vacancy radius accounts for all atomic relaxations around the vacancy. If we were to define this radius from the cation-vacancy bond distance only, the result would be the opposite; i.e., $r_V > r_O$! The use of MD and DFT simulations has therefore provided, for the first time, an atomistic explanation of lattice relaxations for Hong & Virkar's (41) observation that vacancies behave as particles with a radius smaller than that of the oxide ion. These simulations also provide a way to form estimates of the vacancy radius prior to experimental confirmation. Indeed, the obtained value of $r_V = 1.07$ Å from **Figure 9** is within 10% of the experimentally derived value obtained by Hong & Virkar (41).

Following this understanding of the atomistic origins of chemical expansion, the expansion due to oxygen vacancies and radii change of cations was predicted from the following equation derived by inserting Equation 16 into Equation 1:

$$\varepsilon = \frac{a - a_0}{a_0} = \frac{[r_M - r_{Ce} - 0.25r_O + 0.25r_V]}{r_{Ce} + r_O}x = \left[\frac{r_M - r_{Ce}}{r_{Ce} + r_O} + \frac{1}{4}\frac{r_V - r_O}{r_{Ce} + r_O}\right]x = (\alpha_M + \alpha_V)x = \alpha_C x, \quad 17.$$

where α_M and α_V are the cation and vacancy stoichiometric expansion coefficients, respectively. It is now clear why the critical radius (discussed in the previous section) of ceria is bigger than the radius of Ce^{4+}: To achieve zero chemical expansion, the radius of the dopant cation has to compensate for the small lattice contraction around a vacancy. Equation 17 also shows that, in principle, there are two ways of reducing the chemical expansion coefficient of ceria, namely decreasing α_M and decreasing α_V.

Recently, the concept of controlling α_V was used to demonstrate a reduced α_C of a ceria through the addition of zirconium. The underlying idea was that ceria and zirconia have different vacancy

radii (r_V = 1.164 and 0.993 Å, respectively), which leads to different values of α_V (−0.023 and −0.044, respectively). Assuming that α_V has an intermediate value in a ceria-zirconia solid solution, and because only cerium reduces, the resulting chemical expansion coefficient, α_C, is smaller (see Equation 17). A combination of dilatometry and XRD experiments at different temperatures, together with DFT calculations, confirmed this finding; the chemical expansion coefficient of this material was ∼50% smaller than in ceria alone. More recently, the dependence of r_V on the host cation radius was systematically studied and showed a larger value for host cations closer to the ionic radius of cerium compared with the case of much smaller cations, such as hafnium and zirconium (42).

5.4. Additional Factors Contributing to the Stoichiometry Expansion Coefficient

The above discussion reasonably makes significant use of Shannon ionic radii in studying the origins of chemical expansion (62). However, many of the perovskite materials in **Table 3** exhibit metal-like conductivity behavior, indicative of electron delocalization and hence of a deviation from the assumptions underlying Shannon radii (62). Indeed, charge delocalization decreased α_C in simulated fluorite and perovskite oxides (43) and was experimentally demonstrated (123). Defects are also expected to interact considerably in large concentrations (133, 134), especially when one considers the several-unit-cell distance over which lattice relaxation occurs for a single oxygen vacancy (42). For large dopant concentrations (>∼10–20 mol%) or nonstoichiometry, the rate of lattice expansion with increasing oxygen vacancy concentration decreases (95, 135, 136). Defects may form short-range groups, known as defect complexes or associates, with reduced volume (95, 135, 137, 138).

6. IMPACT OF STOICHIOMETRIC EXPANSION ON OTHER MECHANICAL PROPERTIES

In addition to the expansion that materials undergo with changes in defect concentration, there are often corresponding changes in other mechanical properties such as elastic modulus and fracture strength. Additionally, strain-driven rearrangements of oxygen vacancies at or near room temperature may explain anomalous elastic behavior (139). **Figure 10*a*** shows an example of the decrease in the elastic moduli of ceria and $Gd_{0.1}Ce_{0.9}O_{1.95-\delta}$ (GDC) upon exposure to reducing conditions with consequent loss of oxygen, as opposed to the case for YSZ, which exhibits no change in δ over the studied range and thus has a constant modulus (5). Later in situ measurements in **Figure 10*b*** display a similar trend (7). The decrease in modulus upon stoichiometric expansion results from the lengthening and corresponding weakening of bonds. The bond energy (U) between atoms in a crystal may be approximated by the following generalized version of the well-known Lennard-Jones potential:

$$U = \frac{b_r}{r^n} - \frac{b_a}{r^m}. \qquad 18.$$

Here, r is the interatomic distance (between a nearest-neighbor cation and anion); b_r and b_a are empirically determined constants for the repulsive and attractive components of the ionic bond energy in a perfect (defect-free) crystal, respectively; n is the Born exponent; and m arises from the Coulombic (attractive) forces. The elastic modulus (E) can be estimated from the second derivative of Equation 18 evaluated at $r = r_{eq}$, the equilibrium interatomic distance (34, 35),

$$E = \frac{1}{r_{eq}} \frac{\partial^2 U}{\partial r^2}\bigg|_{r=r_{eq}} = b_r n (n-m) \frac{1}{r_{eq}^{n+3}} = b_a m (n-m) \frac{1}{r_{eq}^{m+3}}, \qquad 19.$$

which has a solution for both repulsion- and attraction-dominated forces.

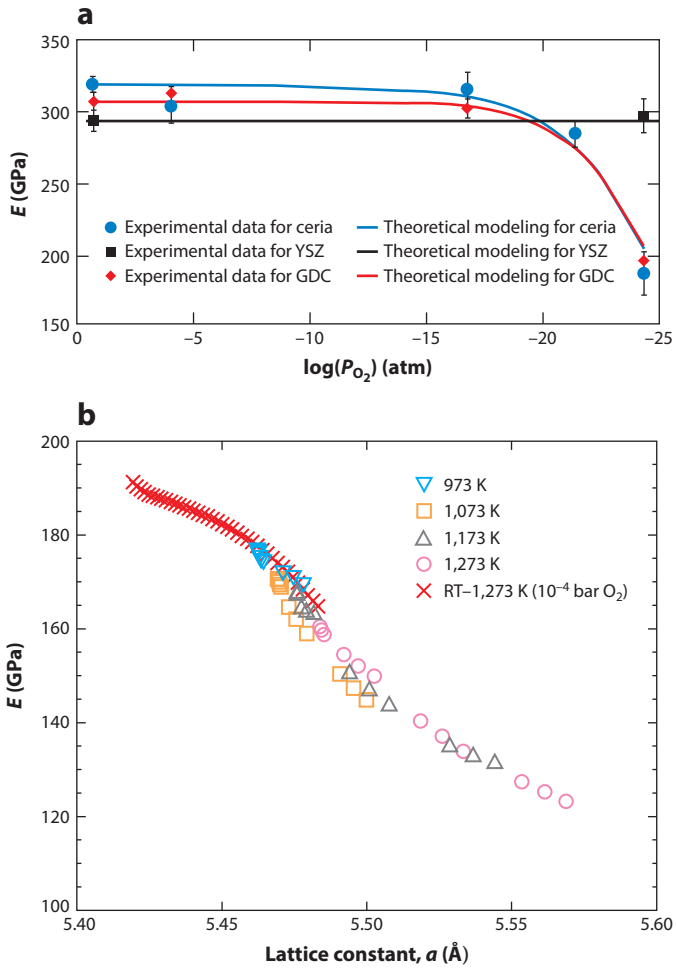

Figure 10

(*a*) Elastic moduli of CeO_2, $Gd_{0.1}Ce_{0.9}O_{1.95-\delta}$ (GDC), and yttria-stabilized zirconia (YSZ) after equilibration at the indicated oxygen partial pressure (P_{O_2}) values at 800°C followed by quenching to room temperature (*points*) with the model given by Equation 20 (*line*). (*b*) In situ elastic modulus measurements of GDC showing a dependence on lattice parameter. RT denotes room temperature. Reprinted with permission from References 5 and 7.

For the fluorite structure, $r_{eq} = \sqrt{3}a/4$ (see Equation 13), and $a = a_0 + [V_O^{\bullet\bullet}]\alpha_0 a_0$ (see Equation 1), where a_0 is the lattice parameter of the stoichiometric compound. Combining these results with Equation 19 yields

$$E = E^* \left(\alpha_C [V_O^{\bullet\bullet}] + 1\right)^{-(n+3)}, \quad \text{where} \quad E^* = b_r n (n-m) \left(\frac{\sqrt{3}}{4} a_0\right)^{-(n+3)}, \qquad 20a.$$

or, analogously,

$$E = E^* \left(\alpha_C [V_O^{\bullet\bullet}] + 1\right)^{-(m+3)}, \quad \text{where} \quad E^* = b_a m (n-m) \left(\frac{\sqrt{3}}{4} a_0\right)^{-(m+3)}. \qquad 20b.$$

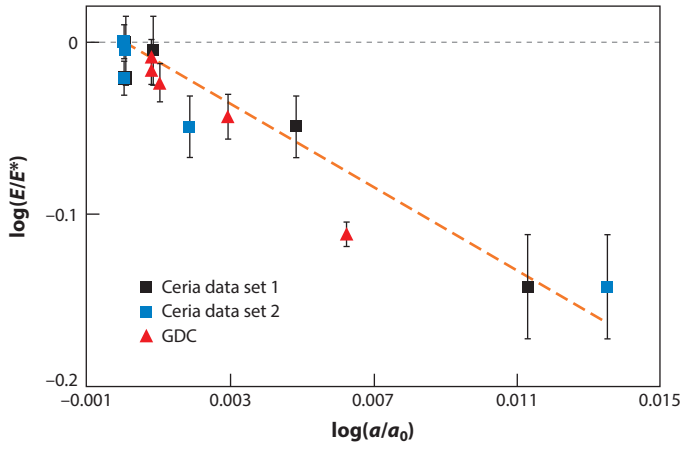

Figure 11

Normalized elastic modulus (E/E^*) as a function of the normalized lattice parameter (a/a_0) for $Gd_{0.1}Ce_{0.9}O_{1.95-\delta}$ (GDC) and two data sets of ceria. The dashed orange line has a slope of $q = 9$ in Equation 21. Reprinted with permission from Reference 5.

Equation 20 provides a direct link between the modulus and chemical expansion; E^* can be considered the modulus in the absence of chemical expansion (e.g., in air for GDC). One also needs to take into consideration that b_r and b_a may vary with defect population. By incorporating a defect model for oxygen vacancy concentration (similar to Equation 8), one can further obtain the functional dependence of the elastic modulus on point defect concentration and P_{O_2}, as shown in **Figure 10*a***. The ability to input unchanged parameters from independent experiments (e.g., defect formation energies and α_C) in Equation 20 demonstrates the validity of the approach and the important role played by defects in the thermomechanical properties of ceramics.

Fitting the elastic modulus data with Equation 20b by using $m = 1$ (typical for ceramics) resulted in an overestimation of the elastic modulus of ceria (35). Therefore, investigators (35) concluded that changes in the repulsive component, b_r, arising from increasing the point defect concentration have a greater influence on the bond energy than do corresponding changes in the attractive component, b_a. Hence Equation 20a provides a more appropriate model for the dependence of elastic modulus on point defect concentration.

A relationship between the modulus and the lattice parameter of the chemically reduced sample relative to the unreduced sample can be introduced as

$$\frac{E}{E^*} = \left(\frac{a}{a_0}\right)^{-(q+3)}. \qquad 21.$$

Here q is either n or m, depending on whether Equation 20a or Equation 20b is adopted, respectively, and the slope of the logarithm of this relationship indicates the mechanism that dominates the modulus-expansion relationship.

To evaluate the exponent in Equation 21, the lattice parameter values for CeO_2 and GDC by Chiang et al. (106) and Wang et al. (140) (which reported that powder materials were heat treated under conditions similar to those yielding the data in **Figure 10**) were plotted in **Figure 11**. The values for E^* and a_0 were taken as the elastic modulus and the lattice parameter for air-treated pure ceria, respectively (4). The data can be fitted very well with the line corresponding to slope q, which, in turn, is approximately identical to the value of n used for modeling the attractive component

Table 4 Room-temperature flexural strength of ceria. Data from Reference 8

Approximate composition	Heat treatment condition	P_{O_2} (atm)	σ_f (MPa)
$CeO_{1.825}$	H_2	4.8×10^{-24}	<4
$CeO_{1.877}$	H_2/H_2O	2.3×10^{-22}	8–9
$CeO_{1.991}$	H_2/H_2O/Ar	8.8×10^{-20}	41 ± 4
CeO_2	Ar	3.4×10^{-4}	137 ± 8
CeO_2	Air	0.21	113 ± 19

of the Lennard-Jones potential above and further indicates that Equation 20a is appropriate for the description of the elastic modulus of CeO_2.

The fracture properties, flexural strength (σ_f), and fracture toughness (K_{1C}) of $CeO_{2-\delta}$ treated in a manner similar to that described above were also investigated (8). **Table 4** shows the dramatic reduction in σ_f with decreasing P_{O_2} treatment at 800°C from 113 MPa in air to <4 MPa in H_2. This decrease can be explained in terms of the reduction in modulus with decreasing P_{O_2} because σ_f is proportional to $E^{1/2}$. However, the fracture toughness surprisingly appears to increase slightly with decreasing P_{O_2} (**Table 5**) because K_{1C} is also proportional to $E^{1/2}$. This increase in fracture toughness has been attributed to extensive microcracking of the reduced samples, resulting in crack deflection mechanisms, essentially microcrack toughening (8).

7. PREDICTIVE STRESS MODELING OF CHEMICAL EXPANSION

Owing to the fact that the devices discussed above are often exposed to large, steady-state or time-dependent gradients in chemical or electrochemical potentials, with corresponding gradients in defect concentration, significant defect-induced stresses, arising from chemical expansion, can develop (56, 141).

In SOFCs and OPMs, for example, the gradient in P_{O_2} across the dense, nonstoichiometric oxide membrane results in a gradient in oxygen vacancy concentration and corresponding stoichiometric expansion. Typically, such a membrane is physically constrained, thus leading to a stress profile that during use depends on (*a*) α_C, (*b*) defect thermodynamic and transport parameters of the membrane, (*c*) mechanical properties of the membrane, (*d*) conditions of operation (temperature and P_{O_2} at each side), (*e*) electrode polarization resistances, and (*f*) geometric characteristics such as membrane thickness. The last three parameters (*d–f*), which are independent of the membrane material, can be exploited to reduce the risk of mechanical failure. For example, at 900°C and permeate-side $P_{O_2} = 10^{-19}$ atm, the strain encountered under operation of a 30-μm $Ce_{0.9}Gd_{0.1}O_{1.95-\delta}$ thin-film membrane, limited primarily by oxygen transport and exchange at electrodes (condition *e* above), was assessed to be six times less than that for the corresponding thicker material limited by diffusion and in equilibrium with the permeate gas while maintaining

Table 5 Room-temperature fracture toughness of ceria. Data from Reference 8

Approximate composition	Heat treatment condition	P_{O_2} (atm)	K_{1C} (MPa)
$CeO_{1.78}$	H_2	8.5×10^{-26}	—
$CeO_{1.899}$	H_2/H_2O	4.5×10^{-22}	1.27–1.36
$CeO_{1.981}$	H_2/H_2O	1.5×10^{-20}	1.40–1.39
CeO_2	Air	0.21	0.95 ± 0.06

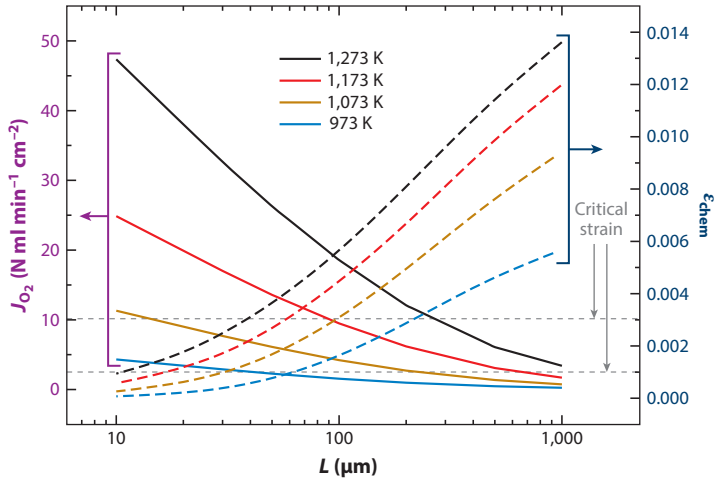

Figure 12

Calculated oxygen flux and chemical strain, ε_{chem} (associated with stoichiometric expansion), as a function of the thickness of a $Ce_{0.9}Gd_{0.1}O_{1.95-\delta}$-based membrane. The horizontal dotted gray lines represent critical ε_{chem} values of 0.001 and 0.003 that correspond to channel cracking and buckling modes of failure, respectively. For membrane thicknesses less than the crossover values between these lines and the lines representing the dependence of ε_{chem} on thickness at each temperature, the membrane is expected to be mechanically stable with respect to the considered failure mechanisms. Reproduced from Reference 143 with permission from The Electrochemical Society.

an oxygen flux of more than 16 N ml min^{-1} cm^{-2} (142). Control of the membrane thickness thus provides a means for reducing the established strain while enhancing the OPM performance (143), as shown by **Figure 12**. Additionally, maximum acceptable strain levels of ~0.1–0.3%, depending on the expected failure mode, have been predicted (144, 145) and are indicated in **Figure 12**.

For SOFC applications, several authors have developed models to predict both the steady-state stresses and time-dependent stresses in membranes and electrode materials that exhibit nonstoichiometry during operation (18, 21, 141, 146–148). As in the OPM case, Krishnamurthy & Sheldon (18) highlighted the role of oxygen surface exchange coefficient compared with the role of bulk diffusion, demonstrating that, at low temperature for thin electrolytes, surface exchange limits oxygen transport, resulting in little to no gradient in oxygen activity and hence a reduced gradient in stress.

Recent work by Woodford et al. (19, 71) demonstrated the importance of developing criteria for mechanical failure in materials for lithium ion batteries, such as $LiCoO_2$. By combining micromechanical models with in situ acoustic emission experiments, the authors found that minimizing principal shear strain (i.e., the anisotropy of chemical expansion), rather than volumetric chemical expansion, is an important design criterion. They also found that polycrystalline particles of anisotropic lithium-storage materials should be synthesized with primary crystallite sizes smaller than a materials-specific critical size to avoid fracture along grain boundaries (19, 71).

8. USING CHEMICAL EXPANSION TO PROBE OR CONTROL OTHER PROPERTIES

As discussed throughout this article, chemical expansion has often been regarded as a deleterious property of, for example, battery and SOFC materials. However, over the past few years,

researchers have begun to take advantage of chemical expansion as a means to indirectly probe other materials properties. For example, Moreno et al. (12) recently probed the rate of oxygen exchange across the gas/solid interface, a key figure of merit in SOFC electrodes, by using high-temperature XRD (HTXRD) to monitor subtle changes in lattice parameter induced by changes in the oxygen stoichiometry of $La_2NiO_{4+\delta}$ thin films and of $La_2NiO_{4+\delta}/LaNiO_3$ bilayers following a step change in P_{O_2}. Unlike more traditional electrical conductivity relaxation and isotopic exchange depth-profiling approaches, HTXRD is a contactless and nondestructive technique. Additionally, in situ studies of relaxation of thin-film curvature (13) and dilatometry of bulk ceramics (14) have been employed to study oxygen exchange across the gas/solid interface and transport in the bulk, respectively.

A great deal of attention has recently been directed toward the local probing of redox reactions involving ion transport at materials' surfaces and interfaces. One example is the use of scanning transmission electron microscopy to spatially map lattice parameter and, in turn, oxygen vacancy concentration variations (10). Additionally, the novel technique of electrochemical strain microscopy has emerged as a powerful tool for localized probing of oxygen reduction and evolution (9) and lithium intercalation in battery materials (11). Lastly, applied stress/strain was demonstrated to induce changes in oxygen content of materials and was applied to induce the metal-to-insulator transition in $NiO_{1-\delta}$ for electroresistive switching applications (149, 150).

SUMMARY POINTS

1. Chemical expansion is the change in a material's dimensions upon a change in its composition and is generally observed in many classes of ceramics and metals, including materials for SOFCs, batteries, and hydrogen storage.
2. Stoichiometric expansion and phase change expansion represent two classes of chemical expansion related to volumetric changes, with gradual changes in composition in the former and significant structural changes in the latter.
3. Both experimental and computational simulation approaches have shown that stoichiometric expansion is tied to the formation of point defects, with a complex dependence on the local relaxations in their neighborhood, and is thus very sensitive to symmetry and atomic arrangement within the unit cell.
4. Chemical expansion has severe implications for the mechanical durability of energy conversion and storage devices.
5. Recent work has demonstrated the use of chemical expansion as a means to probe other materials properties.
6. Through electrochemomechanical coupling, chemical expansion can emerge as an important parameter in controlling materials functionality.

FUTURE ISSUES

1. There remains an opportunity to uncover the atomistic origins of chemical expansion and associated defect relaxations in energy materials such as batteries, as well as an opportunity to extend the rigorous studies of fluorite materials discussed above to perovskite oxides.

2. Although bulk materials have received intense study, the role of interfaces and nanoscale morphology on chemical expansion, particularly as devices progress toward smaller dimensions, will become an intriguing topic.
3. With a better understanding of the relationship between chemical expansion and materials composition, further development of chemical expansion as a tool by which to probe materials properties is expected.
4. The derivation of new methods to reduce the chemical expansion coefficient, thereby overcoming mechanical instabilities, is an ever-present challenge.
5. Chemical expansion needs to play a more central role in modeling of energy conversion and storage devices due to its key role in device durability.
6. Future work is needed to fully establish and understand the relationship between chemical expansion (and associated strain) in device components and their mechanical and electrochemical properties.

DISCLOSURE STATEMENT

The authors are not aware of any affiliations, memberships, funding, or financial holdings that might be perceived as affecting the objectivity of this review.

ACKNOWLEDGMENTS

SRB and NHP acknowledge support from WPI-I2CNER, sponsored by MEXT, Japan. HLT, SRB, NHP, and DM gratefully acknowledge support from the US Department of Energy Basic Energy Sciences Small Group Research Program (J. Vetrano, Program Officer), grant DE-SC0002633. DM thanks the Government of Ireland for an EMPOWER postdoctoral fellowship. CC thanks the Catalysis for Sustainable Energy (CASE) initiative funded by the Danish Ministry of Science, Technology and Innovation for support.

LITERATURE CITED

1. Miller-Chou BA, Koenig JL. 2003. A review of polymer dissolution. *Prog. Polym. Sci.* 28:1223–70
2. Young D. 2008. *High Temperature Oxidation and Corrosion of Metals*. Oxford, UK: Elsevier
3. Ding H, Virkar AV, Liu M, Liu F. 2013. Suppression of Sr surface segregation in $La_{1-x}Sr_xCo_{1-y}Fe_yO_{3-\delta}$: a first principles study. *Phys. Chem. Chem. Phys.* 15:489–96
4. Lee W, Han JW, Chen Y, Cai Z, Yildiz B. 2013. Cation size mismatch and charge interactions drive dopant segregation at the surfaces of manganite perovskites. *J. Am. Chem. Soc.* 135:7909–25
5. Wang Y, Duncan K, Wachsman ED, Ebrahimi F. 2007. The effect of oxygen vacancy concentration on the elastic modulus of fluorite-structured oxides. *Solid State Ionics* 178:53–58
6. Kimura Y, Kushi T, Hashimoto S, Amezawa K, Kawada T. 2012. Influences of temperature and oxygen partial pressure on mechanical properties of $La_{0.6}Sr_{0.4}Co_{1-y}Fe_yO_{3-\delta}$. *J. Am. Ceram. Soc.* 95:2608–13
7. Amezawa K, Kushi T, Sato K, Unemoto A, Hashimoto S, Kawada T. 2011. Elastic moduli of $Ce_{0.9}Gd_{0.1}O_{2-\delta}$ at high temperatures under controlled atmospheres. *Solid State Ionics* 198:32–38
8. Wang Y, Duncan KL, Wachsman ED, Ebrahimi F. 2007. Effects of reduction treatment on fracture properties of cerium oxide. *J. Am. Ceram. Soc.* 90:3908–14
9. Kumar A, Leonard D, Jesse S, Ciucci F, Eliseev EA, et al. 2013. Spatially resolved mapping of oxygen reduction/evolution reaction on solid-oxide fuel cell cathodes with sub–10 nm resolution. *ACS Nano* 7:3808–14

10. Kim Y, He J, Biegalski MD, Ambaye H, Lauter V, et al. 2012. Probing oxygen vacancy concentration and homogeneity in solid-oxide fuel-cell cathode materials on the subunit-cell level. *Nat. Mater.* 11:888–94
11. Balke N, Jesse S, Morozovska AN, Eliseev E, Chung DW, et al. 2010. Nanoscale mapping of ion diffusion in a lithium-ion battery cathode. *Nat. Nanotechnol.* 5:749–54
12. Moreno R, Garcia P, Zapata J, Roqueta J, Chaigneau J, Santiso J. 2013. Chemical strain kinetics induced by oxygen surface exchange in epitaxial films explored by time-resolved X-ray diffraction. *Chem. Mater.* 25:3640–47
13. Yang Q, Burye TE, Lunt RR, Nicholas JD. 2013. In situ oxygen surface exchange coefficient measurements on lanthanum strontium ferrite thin films via the curvature relaxation method. *Solid State Ionics* 249–250:123–28
14. Bishop SR, Kim JJ, Thompson N, Chen D, Kuru Y, et al. 2011. Mechanical, electrical, and optical properties of $(Pr,Ce)O_2$ solid solutions: kinetic studies. *ECS Trans.* 35:1137–44
15. Chatzichristodoulou C, Hendriksen PV, Hagen A. 2010. Defect chemistry and thermomechanical properties of $Ce_{0.8}Pr_xTb_{0.2-x}O_{2-\delta}$. *J. Electrochem. Soc.* 157:B299–307
16. Bishop SR, Tuller HL, Kuru Y, Yildiz B. 2011. Chemical expansion of nonstoichiometric $Pr_{0.1}Ce_{0.9}O_{2-\delta}$: correlation with defect equilibrium model. *J. Eur. Ceram. Soc.* 31:2351–56
17. Beaulieu L, Eberman K, Turner R, Krause L, Dahn J. 2001. Colossal reversible volume changes in lithium alloys. *Electrochem. Solid State Lett.* 4:A137–40
18. Krishnamurthy R, Sheldon BW. 2004. Stresses due to oxygen potential gradients in non-stoichiometric oxides. *Acta. Mater.* 52:1807–22
19. Woodford WH, Carter WC, Chiang YM. 2012. Design criteria for electrochemical shock resistant battery electrodes. *Energy Environ. Sci.* 5:8014–24
20. Atkinson A, Ramos TMGM. 2000. Chemically-induced stresses in ceramic oxygen ion–conducting membranes. *Solid State Ionics* 129:259–69
21. Swaminathan N, Qu J, Sun Y. 2007. An electrochemomechanical theory of defects in ionic solids. I. Theory. *Philos. Mag.* 87:1705–21
22. Kushima A, Yildiz B. 2010. Oxygen ion diffusivity in strained yttria stabilized zirconia: Where is the fastest strain? *J. Mater. Chem.* 20:4809–19
23. Garcia-Barriocanal J, Rivera-Calzada A, Varela M, Sefrioui Z, Iborra E, et al. 2008. Colossal ionic conductivity at interfaces of epitaxial ZrO_2:Y_2O_3/$SrTiO_3$ heterostructures. *Science* 321:676–80
24. Schichtel N, Korte C, Hesse D, Janek J. 2009. Elastic strain at interfaces and its influence on ionic conductivity in nanoscaled solid electrolyte thin films—theoretical considerations and experimental studies. *Phys. Chem. Chem. Phys.* 11:3043–48
25. De Souza RA, Ramadan A, Hoerner S. 2012. Modifying the barriers for oxygen-vacancy migration in fluorite-structured CeO_2 electrolytes through strain: a computer simulation study. *Energy Environ. Sci.* 5:5445–53
26. Rushton MJD, Chroneos A, Skinner SJ, Kilner JA, Grimes RW. 2013. Effect of strain on the oxygen diffusion in yttria and gadolinia co-doped ceria. *Solid State Ionics* 230:37–42
27. Fabbri E, Pergolesi D, Traversa E. 2010. Ionic conductivity in oxide heterostructures: the role of interfaces. *Sci. Technol. Adv. Mater.* 11:054503
28. Burbano M, Marrocchelli D, Watson GW. 2013. Strain effects on the ionic conductivity of Y-doped ceria: a simulation study. *J. Electroceram.* doi:10.1007/s10832-013-9868-y
29. Kalinin SV, Spaldin NA. 2013. Functional ion defects in transition metal oxides. *Science* 341:858–59
30. Jiang J, Hertz J. 2014. On the variability of reported ionic conductivity in nanoscale YSZ thin films. *J. Electroceram.* 32:37–46
31. Kossoy A, Frenkel AI, Wang Q, Wachtel E, Lubomirsky I. 2010. Local structure and strain-induced distortion in $Ce_{0.8}Gd_{0.2}O_{1.9}$. *Adv. Mater.* 22:1659–62
32. Tuller HL, Bishop SR. 2011. Point defects in oxides: tailoring materials through defect engineering. *Annu. Rev. Mater. Res.* 41:369–98
33. Swallow JG, Woodford W, Chen Y, Lu Q, Kim JJ, et al. 2014. Chemomechanics of ionically conductive ceramics for electrical energy conversion and storage. *J. Electroceram.* 32:3–27
34. Duncan KL, Wang Y, Bishop SR, Ebrahimi F, Wachsman ED. 2006. Role of point defects in the physical properties of fluorite oxides. *J. Am. Ceram. Soc.* 89:3162–66

35. Duncan KL, Wang Y, Bishop SR, Ebrahimi F, Wachsman ED. 2007. The role of point defects in the physical properties of nonstoichiometric ceria. *J. Appl. Phys.* 101:044906
36. Merriam-Webster. 2013. *Definition of stoichiometry*. **http://www.merriam-webster.com/dictionary/stoichiometry**
37. Bevan DJM. 1955. Ordered intermediate phases in the system CeO_2-Ce_2O_3. *J. Inorg. Nucl. Chem.* 1:49–59
38. Brauer G, Gingerich KA. 1960. Über die Oxyde des Cers. V. Hochtemperatur-Röntgenuntersuchungen an ceroxyden. *J. Inorg. Nucl. Chem.* 16:87–99
39. Manes L, Parteli E, Mari CM. 1981. A new statistical thermodynamic theory for substoichiometric fluorite structure compounds and its application. 2. Spinoidal points in the G-curves of substoichiometric fluorite structure compounds. *Mater. Chem.* 6:401–15
40. Kim D-J. 1989. Lattice parameters, ionic conductivities, and solubility limits in fluorite-structure MO_2 oxide [M = Hf^{4+}, Zr^{4+}, Ce^{4+}, Th^{4+}, U^{4+}] solid solutions. *J. Am. Ceram. Soc.* 72:1415–21
41. Hong SJ, Virkar AV. 1995. Lattice parameters and densities of rare-earth oxide doped ceria electrolytes. *J. Am. Ceram. Soc.* 78:433–39
42. Marrocchelli D, Bishop SR, Kilner J. 2013. Chemical expansion and its dependence on the host cation radius. *J. Mater. Chem. A* 1:7673–80
43. Marrocchelli D, Bishop SR, Tuller HL, Watson GW, Yildiz B. 2012. Charge localization increases chemical expansion in cerium-based oxides. *Phys. Chem. Chem. Phys.* 14:12070–74
44. Marrocchelli D, Bishop SR, Tuller HL, Yildiz B. 2012. Understanding chemical expansion in non-stoichiometric oxides: ceria and zirconia case studies. *Adv. Funct. Mater.* 22:1958–65
45. Vegard L. 1921. Die Konstitution der Mischkristalle und die Raumfullung der Atome. *Z. Phys.* 5:17–26
46. Mogensen M, Sammes NM, Tompsett GA. 2000. Physical, chemical and electrochemical properties of pure and doped ceria. *Solid State Ionics* 129:63–94
47. Larsen PH, Hendriksen PV, Mogensen M. 1997. Dimensional stability and defect chemistry of doped lanthanum chromites. *J. Therm. Anal.* 49:1263–75
48. Chen XY, Yu JS, Adler SB. 2005. Thermal and chemical expansion of Sr-doped lanthanum cobalt oxide ($La_{1-x}Sr_xCoO_{3-\delta}$). *Chem. Mater.* 17:4537–46
49. Singhal SC, Kendall K. 2003. *High Temperature Solid Oxide Fuel Cells: Fundamentals, Design, and Applications*. Oxford, UK/New York: Elsevier. 1st ed.
50. Minh NQ, Takahashi T. 1995. *Science and Technology of Ceramic Fuel Cells*. Amsterdam: Elsevier
51. Stiller C, Thorud B, Seljebø S, Mathisen Ø, Karoliussen H, Bolland O. 2005. Finite-volume modeling and hybrid-cycle performance of planar and tubular solid oxide fuel cells. *J. Power Sourc.* 141:227–40
52. Demirbas A. 2007. Progress and recent trends in biofuels. *Prog. Energy Combust. Sci.* 33:1–18
53. Mogensen M, Lindegaard T, Hansen U, Mogensen G. 1994. Physical properties of mixed conductor solid oxide fuel cell anodes of doped CeO_2. *J. Electrochem. Soc.* 141:2122–28
54. Sato K, Yashiro K, Kawada T, Yugami H, Hashida T, Mizusaki J. 2010. Fracture process of nonstoichiometric oxide based solid oxide fuel cell under oxidizing/reducing gradient conditions. *J. Power Sourc.* 195:5481–86
55. Bishop SR, Duncan KL, Wachsman ED. 2010. Thermo-chemical expansion in strontium-doped lanthanum cobalt iron oxide. *J. Am. Ceram. Soc.* 93:4115–21
56. Frade JR. 2013. Challenges imposed by thermochemical expansion of solid state electrochemical materials. In *Solid Oxide Fuel Cells: Facts and Figures*, ed. JTS Irvine, P Connor, pp. 95–119. London: Springer-Verlag
57. Kreuer KD. 2003. Proton-conducting oxides. *Annu. Rev. Mater. Res.* 33:333–59
58. Hiraiwa C, Han D, Kuramitsu A, Kuwabara A, Takeuchi H, et al. 2013. Chemical expansion and change in lattice constant of Y-Doped $BaZrO_3$ by hydration/dehydration reaction and final heat-treating temperature. *J. Am. Ceram. Soc.* 96:879–84
59. Hatae T, Matsuzaki Y, Yamashita S, Yamazaki Y. 2010. Destruction modes of anode-supported SOFC caused by degrees of electrochemical oxidation in redox cycle. *J. Electrochem. Soc.* 157:B650–54
60. Yang Z, Liu J, Baskaran S, Imhoff CH, Holladay JD. 2010. Enabling renewable energy and the future grid with advanced electricity storage. *J. Mater.* 62:14–23

61. Manthiram A. 2011. Materials challenges and opportunities of lithium ion batteries. *J. Phys. Chem. Lett.* 2:176–84
62. Shannon RD. 1976. Revised effective ionic-radii and systematic studies of interatomic distances in halides and chalcogenides. *Acta Crystallogr. A* 32:751–67
63. Ohzuku T, Kitagawa M, Hirai T. 1990. Electrochemistry of manganese dioxide in lithium nonaqueous cell. 3. X-ray diffractional study on the reduction of spinel-related manganese dioxide. *J. Electrochem. Soc.* 137:769–75
64. Courtney I, Dahn J. 1997. Electrochemical and in situ X-ray diffraction studies of the reaction of lithium with tin oxide composites. *J. Electrochem. Soc.* 144:2045–52
65. Ohzuku T, Iwakoshi Y, Sawai K. 1993. Formation of lithium-graphite intercalation compounds in nonaqueous electrolytes and their application as a negative electrode for a lithium ion (shuttlecock) cell. *J. Electrochem. Soc.* 140:2490–98
66. Whittingham MS, Jacobson AJ, eds. 1982. *Intercalation Chemistry*. New York: Academic
67. Ebert LB. 1976. Intercalation compounds of graphite. *Annu. Rev. Mater. Sci.* 6:181–211
68. Ohzuku T, Ueda A, Yamamoto N. 1995. Zero-strain insertion material of $Li[Li_{1/3}Ti_{5/3}]O_4$ for rechargeable lithium cells. *J. Electrochem. Soc.* 142:1431–35
69. Reimers JN, Dahn JR. 1992. Electrochemical and in situ X-ray diffraction studies of lithium intercalation in Li_xCoO_2. *J. Electrochem. Soc.* 139:2091–97
70. Rönnebro ECE, Majzoub EH. 2013. Recent advances in metal hydrides for clean energy applications. *MRS Bull.* 38:452–58
71. Woodford WH, Chiang Y, Carter WC. 2010. "Electrochemical shock" of intercalation electrodes: a fracture mechanics analysis. *J. Electrochem. Soc.* 157:A1052–59
72. Wu H, Chan G, Choi JW, Ryu I, Yao Y, et al. 2012. Stable cycling of double-walled silicon nanotube battery anodes through solid-electrolyte interphase control. *Nat. Nanotechnol.* 7:309–14
73. Meethong N, Huang HS, Speakman SA, Carter WC, Chiang Y. 2007. Strain accommodation during phase transformations in olivine-based cathodes as a materials selection criterion for high-power rechargeable batteries. *Adv. Funct. Mater.* 17:1115–23
74. Delmas C, Maccario M, Croguennec L, Le Cras F, Weill F. 2008. Lithium deintercalation in $LiFePO_4$ nanoparticles via a domino-cascade model. *Nat. Mater.* 7:665–71
75. Kooi BJ, Zoestbergen E, De Hosson JTM, Kerssemakers JWJ, Dam B, Ward RCC. 2002. Mechanism of the structural phase transformations in epitaxial YH_x switchable mirrors. *J. Appl. Phys.* 91:1901–9
76. Remhof A, Borgschulte A. 2008. Thin-film metal hydrides. *Chem. Phys. Chem.* 9:2440–55
77. Notten PHL, Daams JLC, De Veirman AEM, Staals AA. 1994. In situ X-ray diffraction: a useful tool to investigate hydride formation reactions. *J. Alloy. Compd.* 209:85–91
78. Notten PHL, Daams JLC, Einerhand REF. 1994. On the nature of the electrochemical cycling stability of nonstoichiometric $LaNi_5$-based hydride-forming compounds. 2. In-situ X-ray diffractometry. *J. Alloy. Compd.* 210:233–41
79. Sandrock G. 1999. A panoramic overview of hydrogen storage alloys from a gas reaction point of view. *J. Alloy. Compd.* 293:877–88
80. Huggins RA, Nix WD. 2000. Decrepitation model for capacity loss during cycling of alloys in rechargeable electrochemical systems. *Ionics* 6:57–63
81. Pundt A, Kirchheim R. 2006. Hydrogen in metals: microstructural aspects. *Annu. Rev. Mater. Res.* 36:555–608
82. Alefeld G. 1969. Hydrogen in metals as a model for a lattice gas with phase transformations. *Phys. Status Solid.* 32:67–80
83. Hjorvarsson B, Andersson G, Karlsson E. 1997. Metallic superlattices: quasi two-dimensional playground for hydrogen. *J. Alloy. Compd.* 253:51–57
84. Bindeman I. 2005. Fragmentation phenomena in populations of magmatic crystals. *Am. Miner.* 90:1801–15
85. Sato K, Omura H, Hashida T, Yashiro K, Yugami H, et al. 2006. Tracking the onset of damage mechanism in ceria-based solid oxide fuel cells under simulated operating conditions. *J. Test. Eval.* 34:246–50
86. Didier-Laurent S, Idrissi H, Roue L. 2008. In-situ study of the cracking of metal hydride electrodes by acoustic emission technique. *J. Power Sourc.* 179:412–16

87. Sugiura M. 2003. Oxygen storage materials for automotive catalysts: ceria-zirconia solid solutions. *Catal. Surv. Asia* 7:77–87
88. Gorte RJ. 2010. Ceria in catalysis: from automotive applications to the water gas shift reaction. *AIChe J.* 56:1126–35
89. Cava RJ, Batlogg B, Rabe KM, Rietman EA, Gallagher PK, Rupp LW. 1988. Structural anomalies at the disappearance of superconductivity in $Ba_2YCu_3O_{7-\delta}$: evidence for charge transfer from chains to planes. *Physica C* 156:523–27
90. Farneth WE, Bordia RK, McCarron EM, Crawford MK, Flippen RB. 1988. Influence of oxygen stoichiometry on the structure and superconducting transition temperature of $YBa_2Cu_3O_x$. *Solid State Commun.* 66:953–59
91. Kuru Y, Usman M, Cristiani G, Habermeier HU. 2010. Microstructural changes in epitaxial $YBa_2Cu_3O_{7-\delta}$ thin films due to creation of O vacancies. *J. Cryst. Growth* 312:2904–8
92. Martin R, Omikrine Metalssi O, Toutlemonde F. 2013. Importance of considering the coupling between transfer properties, alkali leaching and expansion in the modelling of concrete beams affected by internal swelling reactions. *Constr. Build. Mater.* 49:23–30
93. Adler SB. 2001. Chemical expansivity of electrochemical ceramics. *J. Am. Ceram. Soc.* 84:2117–19
94. Tuller HL, Nowick AS. 1979. Defect structure and electrical properties of nonstoichiometric CeO_2 single crystals. *J. Electrochem. Soc.* 126:209–17
95. Bishop SR, Duncan KL, Wachsman ED. 2009. Surface and bulk oxygen non-stoichiometry and bulk chemical expansion in gadolinium-doped cerium oxide. *Acta. Mater.* 57:3596–605
96. Wuensch BJ, Tuller HL. 1994. Lattice diffusion, grain-boundary diffusion and defect structure of ZnO. *J. Phys. Chem. Solids* 55:975–84
97. Stratton TG, Tuller HL. 1987. Thermodynamic and transport studies of mixed oxides: the CeO_2-UO_2 system. *J. Chem. Soc. Faraday Trans.* 83:1143–56
98. Choi GM, Tuller HL, Goldschmidt D. 1986. Electronic-transport behavior in single-crystalline $Ba_{0.03}Sr_{0.97}TiO_3$. *Phys. Rev. B* 34:6972–79
99. Choi GM, Tuller HL. 1988. Defect structure and electrical properties of single-crystal $Ba_{0.03}Sr_{0.97}TiO_3$. *J. Am. Ceram. Soc.* 71:201–5
100. Kuhn M, Kim JJ, Bishop SR, Tuller HL. 2013. Oxygen nonstoichiometry and defect chemistry of perovskite-structured $Ba_xSr_{1-x}Ti_{1-y}Fe_yO_{3-y/2+\delta}$ solid solutions. *Chem. Mater.* 25:2970–75
101. Bishop SR, Stefanik TS, Tuller HL. 2012. Defects and transport in $Pr_xCe_{1-x}O_{2-\delta}$: composition trends. *J. Mater. Res.* 27:2009–16
102. Yuan L, Wang Z, Zhang W, Hu X, Chen J, et al. 2011. Development and challenges of $LiFePO_4$ cathode material for lithium-ion batteries. *Energy Environ. Sci.* 4:269–84
103. Andersson A, Kalska B, Haggstrom L, Thomas J. 2000. Lithium extraction/insertion in $LiFePO_4$: an X-ray diffraction and Mössbauer spectroscopy study. *Solid State Ionics* 130:41–52
104. Zhu C, Weichert K, Maier J. 2011. Electronic conductivity and defect chemistry of heterosite $FePO_4$. *Adv. Funct. Mater.* 21:1917–21
105. Mogensen G, Mogensen M. 1993. Reduction reactions in doped ceria ceramics studied by dilatometry. *Thermochim. Acta* 214:47–50
106. Chiang HW, Blumenthal RN, Fournelle RA. 1993. A high-temperature lattice-parameter and dilatometer study of the defect structure of nonstoichiometric cerium dioxide. *Solid State Ionics* 66:85–95
107. Chen X, Grande T. 2013. Anisotropic chemical expansion of $La_{1-x}Sr_xCoO_{3-\delta}$. *Chem. Mater.* 25:927–34
108. Chen X, Grande T. 2013. Anisotropic and nonlinear thermal and chemical expansion of $La_{1-x}Sr_xFeO_{3-\delta}$ ($x = 0.3, 0.4, 0.5$) perovskite materials. *Chem. Mater.* 25:3296–306
109. Grande T, Tolchard JR, Selbach SM. 2012. Anisotropic thermal and chemical expansion in Sr-substituted $LaMnO_{3+\delta}$: implications for chemical strain relaxation. *Chem. Mater.* 24:338–45
110. Mastin J, Einarsrud M, Grande T. 2006. Structural and thermal properties of $La_{1-x}Sr_xCoO_{3-\delta}$. *Chem. Mater.* 18:6047–53
111. Huang KQ, Tichy RS, Goodenough JB. 1998. Superior perovskite oxide-ion conductor; strontium- and magnesium-doped $LaGaO_3$. I. Phase relationships and electrical properties. *J. Am. Ceram. Soc.* 81:2565–75

112. Lu XC, Zhu JH. 2008. Effect of Sr and Mg doping on the property and performance of the $La_{1-x}Sr_xGa_{1-y}Mg_yO_{3-\delta}$ electrolyte. *J. Electrochem. Soc.* 155:B494–503
113. Skowron A, Huang P, Petric A. 1999. Structural study of $La_{0.8}Sr_{0.2}Ga_{0.85}Mg_{0.15}O_{2.825}$. *J. Solid State Chem.* 143:202–9
114. Hayashi H, Suzuki M, Inaba H. 2000. Thermal expansion of Sr- and Mg-doped $LaGaO_3$. *Solid State Ionics* 128:131–39
115. Drennan J, Zelizko V, Hay D, Ciacchi FT, Rajendran S, Badwal SPS. 1997. Characterisation, conductivity and mechanical properties of the oxygen-ion conductor $La_{0.9}Sr_{0.1}Ga_{0.8}Mg_{0.2}O_{3-x}$. *J. Mater. Chem.* 7:79–83
116. Zuev A, Singheiser L, Hilpert K. 2002. Defect structure and isothermal expansion of A-site and B-site substituted lanthanum chromites. *Solid State Ionics* 147:1–11
117. Zuev AY, Sereda VV, Tsvetkov DS. 2012. Defect structure and defect-induced expansion of MIEC oxides: doped lanthanum cobaltites. *J. Electrochem. Soc.* 159:F594–99
118. Zuev AY, Vylkov AI, Petrov AN, Tsvetkov DS. 2008. Defect structure and defect-induced expansion of undoped oxygen deficient perovskite $LaCoO_{3-\delta}$. *Solid State Ionics* 179:1876–79
119. Verma AS, Jindal VK. 2009. Lattice constant of cubic perovskites. *J. Alloy. Compd.* 485:514–18
120. Ubic R, Subodh G. 2009. The prediction of lattice constants in orthorhombic perovskites. *J. Alloy. Compd.* 488:374–79
121. Moreira RL, Dias A. 2007. Comment on "Prediction of lattice constant in cubic perovskites." *J. Phys. Chem. Solids* 68:1617–22
122. Jiang LQ, Guo JK, Liu HB, Zhu M, Zhou X, et al. 2006. Prediction of lattice constant in cubic perovskites. *J. Phys. Chem. Solids* 67:1531–36
123. Perry NH, Thomas JE, Marrocchelli D, Bishop SR, Tuller HL. 2013. Isolating the role of charge localization in chemical expansion: $(La,Sr)(Ga,Ni)O_{3-\delta}$ case study. *ECS Trans.* 57:1879–84
124. Kharton VV, Kovalevsky AV, Avdeev M, Tsipis EV, Patrakeev MV, et al. 2007. Chemically induced expansion of $La_2NiO_{4+\delta}$-based materials. *Chem. Mater.* 19:2027–33
125. Nakamura T, Yashiro K, Sato K, Mizusaki J. 2010. Thermally-induced and chemically-induced structural changes in layered perovskite-type oxides $Nd_{2-x}Sr_xNiO_{4+\delta}$ ($x = 0, 0.2, 0.4$). *Solid State Ionics* 181:402–11
126. Chatzichristodoulou C, Hauback BC, Hendriksen PV. 2013. In situ X-ray and neutron diffraction of the Ruddlesden–Popper compounds $(RE_{2-x}Sr_x)_{0.98}(Fe_{0.8}Co_{0.2})_{1-y}Mg_yO_{4-\delta}$ (RE = La, Pr): structure and CO_2 stability. *J. Solid State Chem.* 201:164–71
127. Andersson DA, Simak SI, Skorodumova NV, Abrikosov IA, Johansson B. 2006. Optimization of ionic conductivity in doped ceria. *Proc. Natl. Acad. Sci. USA* 103:3518–21
128. Omar S, Wachsman ED, Nino JC. 2007. Higher ionic conductive ceria-based electrolytes for solid oxide fuel cells. *Appl. Phys. Lett.* 91:144106
129. Ralph JM, Przydatek J, Kilner J, Seguelong T. 1997. Novel doping systems in ceria. *Ber. Bunsen Phys. Chem.* 101:1403–7
130. Deleted in proof
131. Tuller HL, Nowick AS. 1977. Small polaron electron transport in reduced CeO_2 single crystals. *J. Phys. Chem. Solids* 38:859–67
132. Wang B, Lewis RJ, Cormack AN. 2011. Computer simulations of large-scale defect clustering and nanodomain structure in gadolinia-doped ceria. *Acta Mater.* 59:2035–45
133. Kilner JA, Waters CD. 1982. The effects of dopant cation oxygen vacancy complexes on the anion transport-properties of nonstoichiometric fluorite oxides. *Solid State Ionics* 6:253–59
134. Wachsman ED. 2004. Effect of oxygen sublattice order on conductivity in highly defective fluorite oxides. *J. Eur. Ceram. Soc.* 24:1281–85
135. Omar S, Nino JC. 2013. Consistency in the chemical expansion of fluorites: a thermal revision of the doped ceria. *Acta Mater.* 61:5406–13
136. Inaba H, Tagawa H. 1996. Ceria-based solid electrolytes: review. *Solid State Ionics* 83:1–16
137. Wang B, Cormack AN. 2013. Strain modulation of defect structure in gadolinia-doped ceria. *J. Phys. Chem. C* 117:146–51
138. Bishop SR, Duncan KL, Wachsman ED. 2009. Defect equilibria and chemical expansion in non-stoichiometric undoped and gadolinium-doped cerium oxide. *Electrochim. Acta* 54:1436–43

139. Kossoy A, Wachtel E, Lubomirsky I. 2013. On the Poisson ratio and XRD determination of strain in thin films of $Ce_{0.8}Gd_{0.2}O_{1.9}$. *J. Electroceram.* doi:10.1007/s10832-013-9835-7
140. Wang S, Katsuki M, Dokiya M, Hashimoto T. 2003. High temperature properties of $La_{0.6}Sr_{0.4}Co_{0.8}Fe_{0.2}O_{3-\delta}$ phase structure and electrical conductivity. *Solid State Ionics* 159:71–78
141. Bishop SR. 2013. Chemical expansion of solid oxide fuel cell materials: a brief overview. *Acta Mech. Sin.* 29:312–17
142. Chatzichristodoulou C, Sogaard M, Glasscock J, Kaiser A, Foghmoes SPV, Hendriksen PV. 2011. Oxygen permeation in thin, dense $Ce_{0.9}Gd_{0.1}O_{1.95-\delta}$ membranes. II. Experimental determination. *J. Electrochem. Soc.* 158:F73–83
143. Chatzichristodoulou C, Søgaard M, Hendriksen PV. 2011. Oxygen permeation in thin, dense $Ce_{0.9}Gd_{0.1}O_{1.95-\delta}$ membranes. I. Model study. *J. Electrochem. Soc.* 158:F61–72
144. Hendriksen PV, Høgsberg JR, Kjeldsen AM, Sørensen BF, Pedersen HG. 2007. Failure modes of thin supported membranes. In *Advances in Solid Oxide Fuel Cells II: Ceramic Engineering and Science Proceedings*, ed. NP Bansal, A Wereszczak, E Lara-Curzio, pp. 347–60. New York: Wiley
145. Kaiser A, Foghmoes S, Chatzichristodoulou C, Sogaard M, Glasscock JA, et al. 2011. Evaluation of thin film ceria membranes for syngas membrane reactors: preparation, characterization and testing. *J. Membr. Sci.* 378:51–60
146. Atkinson A. 1997. Chemically-induced stresses in gadolinium-doped ceria solid oxide fuel cell electrolytes. *Solid State Ionics* 95:249–58
147. Terada K, Kawada T, Sato K, Iguchi F, Yashiro K, et al. 2011. Multiscale simulation of electro-chemo-mechanical coupling behavior of PEN structure under SOFC operation. *ECS Trans.* 35:923–33
148. Bishop SR, Tuller HL. 2012. Development of a predictive thermo-chemical expansion and stress model in $(Pr,Ce)O_{2-\delta}$. *ECS Trans.* 41:153–59
149. Kawada T, Masumitsu T, Kimura Y, Watanabe S, Hashimoto S, et al. 2014. Transient shift of local oxygen potential in nonstoichiometric oxides upon application of mechanical stress. *J. Electroceram.* 32:78–85
150. Kim Y, Kelly SJ, Morozovska A, Rahani EK, Strelcov E, et al. 2013. Mechanical control of electroresistive switching. *Nano Lett.* 13:4068–74
151. Nakamura T, Yashiro K, Sato K, Mizusaki J. 2010. Structural analysis of $La_{2-x}Sr_xNiO_{4+\delta}$ by high temperature X-ray diffraction. *Solid State Ionics* 181:292–99
152. Bishop SR, Marrocchelli D, Fang W, Amezawa K, Yashiro K, Watson GW. 2013. Reducing the chemical expansion coefficient in ceria by addition of zirconia. *Energy Environ. Sci.* 6:1142–46
153. McIntosh S, Vente JF, Haije WG, Blank DHA, Bouwmeester HJM. 2006. Oxygen stoichiometry and chemical expansion of $Ba_{0.5}Sr_{0.5}Co_{0.8}Fe_{0.2}O_{3-\delta}$ measured by in situ neutron diffraction. *Chem. Mater.* 18:2187–93
154. Li Y, Maxey ER, Richardson JW Jr, Ma B, Lee TH, Song S. 2007. Oxygen non-stoichiometry and thermal-chemical expansion of $Ce_{0.8}Y_{0.2}O_{1.9-\delta}$ electrolytes by neutron diffraction. *J. Am. Ceram. Soc.* 90:1208–14
155. Magraso A, Hervoches CH, Ahmed I, Hull S, Nordstrom J, et al. 2013. In situ high temperature powder neutron diffraction study of undoped and Ca-doped $La_{28-x}W_{4+x}O_{54+3x/2}$ ($x = 0.85$). *J. Mater. Chem.* 1:3774–82
156. Hull S, Norberg ST, Ahmed I, Eriksson SG, Marrocchelli D, Madden PA. 2009. Oxygen vacancy ordering within anion-deficient ceria. *J. Solid State Chem.* 182:2815–21
157. Valentin O, Millot F, Blond É, Richet N, Julian A, et al. 2011. Chemical expansion of $La_{0.8}Sr_{0.2}Fe_{0.7}Ga_{0.3}O_{3-\delta}$. *Solid State Ionics* 193:23–31
158. Mba JMA, Croguennec L, Basir NI, Barker J, Masquelier C. 2012. Lithium insertion or extraction from/into Tavorite-type $LiVPO_4F$: an in situ X-ray diffraction study. *J. Electrochem. Soc.* 159:A1171–75
159. Schober T, Friedrich J, Triefenbach D, Tietz F. 1997. Dilatometry of the high-temperature proton conductor $Ba_3Ca_{1.18}Nb_{1.82}O_{9-\delta}$. *Solid State Ionics* 100:173–81
160. Kharton VV, Yaremchenko AA, Patrakeev MV, Naumovich EN, Marques FMB. 2003. Thermal and chemical induced expansion of $La_{0.3}Sr_{0.7}(Fe,Ga)O_{3-\delta}$ ceramics. *J. Eur. Ceram. Soc.* 23:1417–26
161. Winter M, Wrodnigg G, Besenhard J, Biberacher W, Novak P. 2000. Dilatometric investigations of graphite electrodes in nonaqueous lithium battery electrolytes. *J. Electrochem. Soc.* 147:2427–31

162. Golovnya AV, Pokrovskii VY. 2003. Interferometric setup for measurements of expansion of whisker-like samples. *Rev. Sci. Instrum.* 74:4418–22
163. Kompan TA, Korenev AS, Pukhov NF, Gurov IP, Dudina TF, Margaryants NB. 2011. The speckle interferometry method for determining the thermal expansion of nanomaterials. *Meas. Tech.* 54:434–41
164. Phillips LC, Kelly RG, Wagner JW, Moran PJ. 1986. An investigation of the volume change associated with discharge of lithium iodine batteries via holographic interferometric techniques. *J. Electrochem. Soc.* 133:1–5
165. Briers JD. 1993. Holographic, speckle and moiré techniques in optical metrology. *Prog. Quant. Electron.* 17:167–233
166. Pan B, Xie H, Hua T, Asundi A. 2009. Measurement of coefficient of thermal expansion of films using digital image correlation method. *Polym. Test.* 28:75–83
167. Malzbender J. 2010. Curvature and stresses for bi-layer functional ceramic materials. *J. Eur. Ceram. Soc.* 30:3407–13
168. Floro JA, Chason E, Lee SR. 1996. Real time measurement of epilayer strain using a simplified wafer curvature technique. *MRS Proc.* 405:381–86
169. Bhatia S, Sheldon BW. 2008. Compositional stresses in polycrystalline titania films. *J. Am. Ceram. Soc.* 91:3986–93
170. Bullard JW III, Smith RL. 2003. Structural evolution of the $MoO_3(010)$ surface during lithium intercalation. *Solid State Ionics* 160:335–49
171. Affoune A, Yamada A, Umeda M. 2005. Conductivity and surface morphology of Nafion membrane in water and alcohol environments. *J. Power Sourc.* 148:9–17
172. Smela E, Gadegaard N. 2001. Volume change in polypyrrole studied by atomic force microscopy. *J. Phys. Chem. B* 105:9395–405
173. Arruda TM, Heon M, Presser V, Hillesheim PC, Dai S, et al. 2013. In situ tracking of the nanoscale expansion of porous carbon electrodes. *Energy Environ. Sci.* 6:225–31
174. Animitsa I, Nieman A, Titova S, Kochetova N, Isaeva E, et al. 2003. Phase relations during water incorporation in the oxygen and proton conductor $Sr_6Ta_2O_{11}$. *Solid State Ionics* 156:95–102
175. Liu L, Lee T, Qiu L, Yang Y, Jacobson A. 1996. A thermogravimetric study of the phase diagram of strontium cobalt iron oxide, $SrCo_{0.8}Fe_{0.2}O_{3-\delta}$. *Mater. Res. Bull.* 31:29–35
176. Mizusaki J, Mima Y, Yamauchi S, Fueki K, Tagawa H. 1989. Nonstoichiometry of the perovskite-type oxides $La_{1-x}Sr_xCoO_{3-\delta}$. *J. Solid State Chem.* 80:102–11
177. Mizusaki J, Yoshihiro M, Yamauchi S, Fueki K. 1985. Nonstoichiometry and defect structure of the perovskite-type oxides $La_{1-x}Sr_xFeO_{3-\delta}$. *J. Solid State Chem.* 58:257–66
178. Chatzichristodoulou C, Hendriksen PV. 2010. Oxygen nonstoichiometry and defect chemistry modeling of $Ce_{0.8}Pr_{0.2}O_{2-\delta}$. *J. Electrochem. Soc.* 157:B481–89
179. Tsvetkov DS, Sereda VV, Zuev AY. 2010. Oxygen nonstoichiometry and defect structure of the double perovskite $GdBaCo_2O_{6-\delta}$. *Solid State Ionics* 180:1620–25
180. Lankhorst MHR, Bouwmeester HJM. 1997. Determination of oxygen nonstoichiometry and diffusivity in mixed conducting oxides by oxygen coulometric titration. 2. Oxygen nonstoichiometry and defect model for $La_{0.8}Sr_{0.2}CoO_{3-\delta}$. *J. Electrochem. Soc.* 144:1268–73
181. Patrakeev MV, Leonidov IA, Kozhevnikov VL. 2011. Applications of coulometric titration for studies of oxygen non-stoichiometry in oxides. *J. Solid State Electrochem.* 15:931–54
182. Birke P, Weppner W. 1997. Electrochemical analysis of thin film electrolytes and electrodes for application in rechargeable all solid state lithium microbatteries. *Electrochim. Acta* 42:3375–84
183. Chen D, Bishop SR, Tuller HL. 2012. Non-stoichiometry in oxide thin films: a chemical capacitance study of the praseodymium-cerium oxide system. *Adv. Funct. Mater.* 23:2168–74
184. Chueh WC, Haile SM. 2009. Electrochemical studies of capacitance in cerium oxide thin films and its relationship to anionic and electronic defect densities. *Phys. Chem. Chem. Phys.* 11:8144–48
185. Jamnik J, Maier J. 2001. Generalised equivalent circuits for mass and charge transport: chemical capacitance and its implications. *Phys. Chem. Chem. Phys.* 3:1668–78
186. Baumann FS, Fleig J, Habermeier HU, Maier J. 2006. Impedance spectroscopic study on well-defined $(La,Sr)(Co,Fe)O_{3-\delta}$ model electrodes. *Solid State Ionics* 177:1071–81

187. Waser R, Bieger T, Maier J. 1990. Determination of acceptor concentrations and energy-levels in oxides using an optoelectrochemical technique. *Solid State Commun.* 76:1077–81
188. Sasaki K, Maier J. 2000. Re-analysis of defect equilibria and transport parameters in Y_2O_3-stabilized ZrO_2 using EPR and optical relaxation. *Solid State Ionics* 134:303–21
189. Kim JJ, Bishop SR, Thompson N, Chen D, Tuller HL. 2014. Investigation of nonstoichiometry in oxide thin films by simultaneous in situ optical absorption and chemical capacitance measurements: Pr doped ceria—case study. *Chem. Mater.* 26:1374–79
190. Liu XH, Huang JY. 2011. In situ TEM electrochemistry of anode materials in lithium ion batteries. *Energy Environ. Sci.* 4:3844–60
191. Wang C, Li X, Wang Z, Xu W, Liu J, et al. 2012. In situ TEM investigation of congruent phase transition and structural evolution of nanostructured silicon/carbon anode for lithium ion batteries. *Nano Lett.* 12:1624–32
192. Chatzichristodoulou C, Schönbeck C, Hagen A, Hendriksen PV. 2013. Defect chemistry, thermomechanical and transport properties of $(RE_{2-x}Sr_x)_{0.98}(Fe_{0.8}Co_{0.2})_{1-y}Mg_yO_{4-\delta}$ (RE = La, Pr). *Solid State Ionics* 232:68–79
193. Armstrong TR, Stevenson JW, Pederson LR, Raney PE. 1996. Dimensional instability of doped lanthanum chromite. *J. Electrochem. Soc.* 143:2919–25
194. Hendriksen PV, Hoegh J, Hansen JR, Larsen PH, Solvang M, et al. 2008. Electrical conductivity and dimensional stability of co-doped lanthanum chromites. *Proc. Electrochem. Soc.* 25:349–67
195. Miyoshi S, Hong J, Yashiro K, Kaimai A, Nigara Y, et al. 2003. Lattice expansion upon reduction of perovskite-type $LaMnO_3$ with oxygen-deficit nonstoichiometry. *Solid State Ionics* 161:209–17
196. Bishop SR, Marrocchelli D, Chatzichristodoulou C. 2014. Defining chemical expansion: the choice of units for the stoichiometric expansion coefficient. *Phys. Chem. Chem. Phys.* In press; doi:10.1039/C4CP01096E